Cement and Concrete Research 151 (2022) 106649

Contents lists available at ScienceDirect

Cement and Concrete Research

journal homepage: www.elsevier.com/locate/cemconres

Degradation mechanism of hybrid fly ash/slag based geopolymers exposed to elevated temperatures

Y. Luo [a], S.H. Li [a], K.M. Klima [a], H.J.H. Brouwers [a], Qingliang Yu [a,b,*]

[a] Department of the Built Environment, Eindhoven University of Technology, P.O. Box 513, 5600MB Eindhoven, the Netherlands
[b] School of Civil Engineering, Wuhan University, 430072 Wuhan, PR China

ARTICLE INFO

Keywords:
Alkali activation
Hybrid binder
Elevated temperature
Microcrack characteristic
Mechanical evolution

ABSTRACT

As a promising alternative to alkali-activated fly ash (AAF) for high temperature application, the degradation mechanism of alkali-activated fly ash/GGBS (AAFS) under high temperature is not clear. This work investigates physicochemical properties of AAFS up to 800 °C and presents their synergetic influence on the thermal behavior. A quantitative assessment of the crack is developed to learn the cracking behavior. Results reveal that the crack density exhibits a linear relationship with ultrasonic pulse velocity. The crack density and compressive strength exhibit a positive correlation before 100 °C, but a negative relationship beyond 100 °C. The addition of slag into geopolymers lessons the geopolymeric behaviors such as further geopolymerization and viscous sintering, but further aggravates the thermal damage owing to the compact structure and unstable hybrid gel. The conceptual models of AAF and AAFS are proposed to explain the degradation mechanism of low slag contained geopolymers under elevated temperatures.

1. Introduction

Alkali-activated fly ash (AAF), also named geopolymer, exhibits significant mechanical property and structural integrity under high-temperature exposure compared to Portland cement (PC) binders [1–3]. For this reason, geopolymers have received the most attention in terms of fire resistance nowadays, which enables a broad range of applications including fire-resistant materials [4–6], thermal insulators [7–9], thermal energy storage concretes [10]. However, for AAF, the energy-consuming high-temperature curing process, as well as the unsatisfied initial strength, largely hinder the further development of its in-situ applications [11]. To counterbalance these limitations, growing attention has been paid to blended alkali-activated fly ash/GGBS binders (AAFS), which combine aluminosilicate source (fly ash or metakaolin) with calcium additives [12–14]. The calcium source from the substitution of slag could not only contribute to the formation of C-(A-)S-H gel, but also partially replace sodium from N-A-S-H gel to form N-C-A-S-H hybrid gel, which results in a higher degree of cross-linking [15–17]. Therefore, the AAFS blends could exhibit a good initial strength with no need of high temperature curing. In terms of high temperature application, different from AAF that exhibits strength gain after elevated temperature exposure, AAFS specimens with higher initial strength eventually exhibit more violent loss of mechanical strength [18–21]. With the increasing addition of slag, AAFS blends exhibit severer weight loss along with more cracks and deteriorations [19,21]. This strength deterioration is highly associated with the physicochemical transformation of AAFS blends. However, up to now, it remains largely unexplored regarding the thermal degradation of AAFS in comparison to that of AAF.

As well known, the evolution of alkaline activated materials under high temperature is a complex process that conjuncts with chemical transformation and physical changes at the same time. Lahito et al. [22,23] reported that, in fly ash based system, two major mechanisms, namely, matrix densification and crack formation, determine the mechanical strengths when exposed to elevated temperatures. The matrix densification favors a strength gain, while the formation of cracks accounts for the loss of strength. However, for AAFS hybrid system, due to the coexistence of N-A-S-H, C-A-S-H or hybrid N-C-A-S-H type gels, their evolution under elevated temperature is more complicated. The mechanical properties of AAFS blends under elevated temperature are both similar to those of AAF and alkali-activated slag. For instance, Park et al. [24] reported the strength gain of AAFS blends before 400 °C is influenced by the further geopolymerization of unreacted fly ash. Pan et al. [18] and Lee et al. [20] concluded that the strength loss of AAFS blends

* Corresponding author at: Department of the Built Environment, Eindhoven University of Technology, P.O. Box 513, 5600MB Eindhoven, the Netherlands.
E-mail address: q.yu@bwk.tue.nl (Q. Yu).

https://doi.org/10.1016/j.cemconres.2021.106649
Received 17 February 2021; Received in revised form 20 October 2021; Accepted 22 October 2021
Available online 29 October 2021

at elevated temperatures is associated with vulnerability of C-(A-)S-H to dehydration and re-crystallization. As a result, the interaction between chemical transformation and physical change on thermal mechanical behavior of AAFS involves in several interactive mechanisms during high temperature exposure, such as further polymerization, dehydration and decomposition, crack formation, re-crystallization and sintering reaction. Nevertheless, very scarce work has systematically connected all the mechanisms and investigated their synergetic influence on the degradation of AAFS blends under high temperatures.

Moreover, it is well acknowledged that the physical change of the AAM matrix caused by cracking would have a direct influence on their further high-temperature performance [25,26]. But, limited data are available concerning the cracking behavior of the AAFS blends under high temperatures. Çelikten et al. [18] found that the depth and number of the cracks in the AAFS mortars increase with the exposure temperature, which further has an adverse impact on their flexural and compressive strength. Dudek et al. [27] compared the cracking behavior between AAFS and AAF mortar, indicating that the AAFS shows larger crack widths and higher crack occurrence frequency as compared to the AAF system under elevated temperatures. In addition, the hybrid AAFS system has a different cracking behavior from sole alkaline activated fly ash or slag materials, which ultimately leads to a different degradation behavior under high-temperature exposure. However, the relationship between cracking behavior and mechanical strength deterioration of AAFS blends that is connected to physicochemical transformations induced by elevated temperatures has not been addressed yet. Moreover, the mechanisms of mechanical evolution of the hybrid AAFS system under elevated temperatures are not well understood either.

The objective of this work is to reveal the mechanism behind the mechanical evolution of AAFS blends under elevated temperatures and clarify the interaction between the concerning competing mechanisms by investigating the synergetic influence of chemical transformation and physical change. A pure fly ash-based paste is introduced as a reference to the hybrid system. To learn the chemical transformation and physical changes of binders exposed to high temperatures under different conditions (20, 100, 200, 400, 600, 800 °C), the chemical properties are evaluated by X-ray diffractometry (XRD), Fourier transform infrared (FTIR) spectroscopy and thermal gravimetric analysis (TGA) analysis. Physical properties including density, pore structure, microstructure, are detected by using pycnometry, mercury intrusion porosimetry (MIP), scanning electron microscopy (SEM) and ultrasonic pulse velocity (UPV) before and after exposure to different temperatures. In addition, to further reveal the mechanical degradation of the hybrid AAFS binder under high temperatures, a quantitative characterization of microcrack based on MATLAB is performed to study their cracking behavior and its influence on the residual strength of AAFS blends.

2. Experimental study

2.1. Materials

The raw materials investigated in this study are Class F fly ash (FA) and ground granulated blast furnace slag (GGBS). FA is commercially purchased from the Netherlands with an average particle size (d_{50}) of 21.09 μm. GGBS with a d_{50} of approximately 19.38 μm is provided by ENCI (IJmuiden, the Netherlands). The particle size distribution of the FA and GGBS is determined by a laser particle size analyzer (Mastersizer 2000, Malvern Instruments, UK), shown in Fig. 1. The chemical composition of the FA and GGBS, as shown in Table 1, is analyzed using X-ray fluorescence spectrometry (XRF) (PANalytical Epsilon 3), and the loss on ignition has been determined from 105 to 1000 °C. The XRD patterns of raw FA and GGBS are shown in Fig. 2. In FA, the presence of crystalline phases quartz (SiO_2) and mullite ($Al_{1.69}Si_{1.22}O_{4.85}$), hematite ($Fe_2O_3$) and magnetite ($Fe_3O_4$) are detected. The GGBS shows several low intensity peaks that are related to anhydrite ($CaSO_4$) and calcite ($CaCO_3$), with a broad amorphous hump between 30° and 40°. Sodium hydroxide pellets (analytical level) and sodium silicate solution (27.69 wt% SiO_2, 8.39 wt% Na_2O, and 63.9 wt% H_2O) are used for alkaline-activator. Distilled water is used to obtain a certain water/binder ratio.

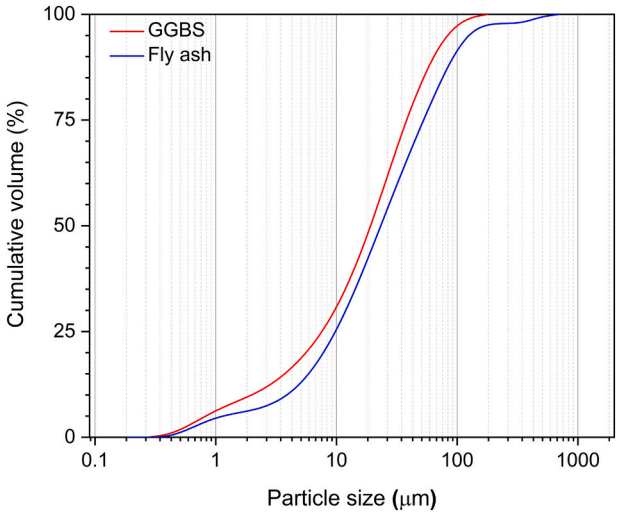

Fig. 1. The particle size distribution of raw materials.

Table 1
Chemical composition of fly ash (FA) and ground granulated blast furnace slag (GGBS).

Oxides (%)	FA	GGBS
SiO_2	53.06	29.41
Al_2O_3	25.23	13.21
CaO	5.27	41.67
MgO	1.05	8.57
Fe_2O_3	8.23	0.37
K_2O	2.01	0.42
SO_3	0.56	2.64
TiO_2	1.61	1.49
Other	0.62	1.07
LOI	2.42	1.15
Specific density (g/cm^3)	2.30	2.93
Specific surface area (m^2/g)	0.82	0.37

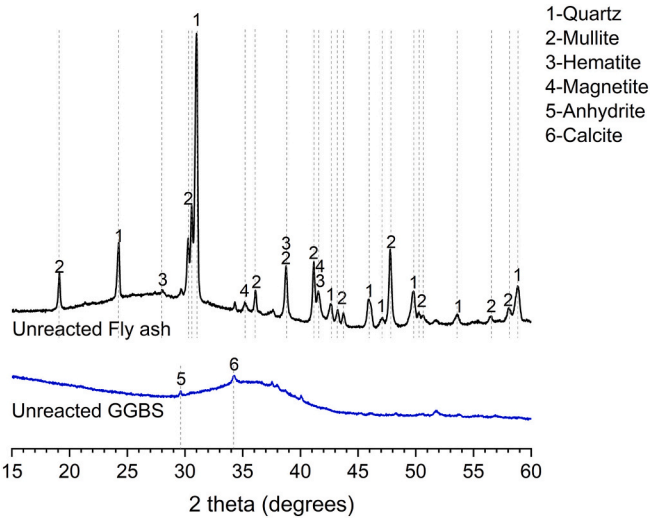

Fig. 2. XRD patterns of GGBS and fly ash.

2.2. Sample preparation

The alkali-activator is synthesized by mixing sodium hydroxide pellets, sodium silicate solution, and distilled water at a certain ratio, and the blended solution is kept at ambient temperature for 1 day prior to use. For all samples, the activator modulus is set constant as 1.4 and the equivalent Na_2O% is kept at 5.6 wt%, because these appeared to be optimum values [28]. The water to solid ratio by mass is 0.35 in all pastes, in which the water consists of the added distilled water as well as the water in sodium silicate solution. The chosen activator modulus, equivalent Na_2O wt%, and water to binder ratio are determined in advance to not only reach a sufficient activation with satisfying flowability but also obtain decent integrity after exposure to elevated temperatures for further characterization.

According to previous works [19,21] and our preliminary experiments, high slag substitution would result in an unstable matrix with drastic inner damage and microstructural change at high temperatures, making the characterization of thermal degradation, especially cracking behavior, more complex. Therefore, the blend weight ratio of FA to slag is set as 95/5 (denoted as AAFS), and a pure FA sample is prepared as reference (denoted as AAF). For the preparation of samples, dried raw materials are firstly mixed by using a 5-l Hobart mixer. When the raw materials reach a homogeneous state, the activator solution is slowly added while stirring. The mixtures are mixed at a low-speed for 30s and another 120 s at a high-speed. The fresh paste is poured into prismatic molds (40 mm × 40 mm × 160 mm) and cubic molds (100 mm × 100 mm × 100 mm). Due to the poor dissolution and low reactivity of FA, a 24 h of 60 °C curing is carried out on sealed AAF pastes according to [29], and AAFS pastes are sealed and kept at room temperature (20.0 ± 2.0 °C). After 24 h, all samples are demoulded and placed at room temperature in a sealed condition for 27 days before characterization.

2.3. Testing methods

In order to investigate the chemical transformations, structural changes, and ultimately reveal their co-influence on the thermal behavior of the geopolymers, series of high-temperature exposure treatment are carried out under 100, 200, 400, 600, 800 °C. Multiple analytical methods are carried on the samples after different temperature treatments to build a picture of the physicochemical transformations as a function of temperature. X-ray diffractometry (XRD), Fourier transform infrared spectroscopy (FT-IR) and Thermogravimetry/differential scanning calorimetry (TG/DSC) are applied for evaluating chemical transformations, while density, Mercury intrusion porosimetry (MIP), scanning electron microscopy (SEM), Ultrasonic pulse velocity (UPV) for structural changes. To prepare the powder samples for XRD, FTIR, and TG-DSC analysis, the unheated samples at the age of 28 days are crushed and immersed in isopropanol for 24 h, and then dried at 40 °C for 24 h to cease the hydration, whereas the thermal exposed samples are tested directly.

2.3.1. Elevated temperature exposure procedure

After 28 days of curing, the obtained pastes are exposed to different temperatures of 100, 200, 400, 600, 800 °C, in a high-temperature oven. In general, the thermal treatment for alkali activated materials remain diverse without a universally accepted protocol, and the heating rate applied in previous studies varying from 1 to 10 °C/min [18,19,21,23,24,30–35]. In this work, with a guarantee of providing a decent structure integrity after elevated temperature exposure for further characterization, a heating rate of 10 °C/min is applied to make the results comparable with previous works. In order to reach a uniform temperature distribution within the specimens, the maximum exposing temperature is kept for 1 h for all samples. The test samples are then naturally cooled down to ambient temperature by opening the vent hole of the furnace. After that, to avoid moisture immersion, all test samples are sealed with plastic film before further characterization. The thermal exposure procedure is shown in Fig. 3, and it should be noted that the cooling process is depicted in dash line representing the schematic instead of actual situation.

2.3.2. X-ray diffraction

The X-ray diffraction characterization is conducted by using a Bruker D4 PHASER for investigating the mineralogical phase changes after exposure to elevated temperatures. All samples are then crushed into powder by ball milling for the test. The parameters are set as time 0.6 s, increment 0.02, scanning range from 10° to 60°, 30 KV by Co tube.

2.3.3. Fourier transform infrared spectroscopy

The Fourier transform infrared spectroscopy (FT-IR) measurement is performed in a Varian 3100 instrument with the wavenumbers ranging from 4000 to 400 cm^{-1} with a resolution of 1 cm^{-1}. The reference samples as well as heated samples are ground prior to the FTIR analysis.

2.3.4. Thermogravimetry/differential scanning calorimetry

Thermogravimetry/differential scanning calorimetry (TG/DSC) analysis is conducted using a STA 449-F1 instrument with a heating rate of 10 °C/min from room temperature to 1000 °C and nitrogen as the carrier gas.

2.3.5. SEM with EDS analyses

To determine the changes in morphology of the specimens under different temperatures and identify their cracking behavior, scanning electron microscopy (SEM, Phenom Pro, The Netherlands) equipped with energy-dispersive spectroscopy (EDS) is applied to analyze samples after exposure to elevated temperatures. The test samples with a thickness of 10 mm are cut from the center of thermally treated pastes and then polished to obtain a smooth and flat surface. In order to minimize the effect of drying shrinkage on matrix, prior to the SEM analysis, the test samples are first immersed in isopropanol for 24 h and subsequent dried at 60 °C for 24 h. The dried sample is then coated with Pt or Au using Quorum 150TS plus sputter coater with a current of 40 mA for 30s. For the cracking behavior study, an image combination method described in Lahoti et al. [22] is applied, as shown in Fig. 4. A surface area of 400 μm × 400 μm at a magnification of 2000× is captured for all tested specimens.

2.3.6. Quantification of microcrack characteristics

An automatic quantification method for the characterization of microcrack length and number of microcracks is developed based on grayscale method inspired by previous studies [36–38]. The script for

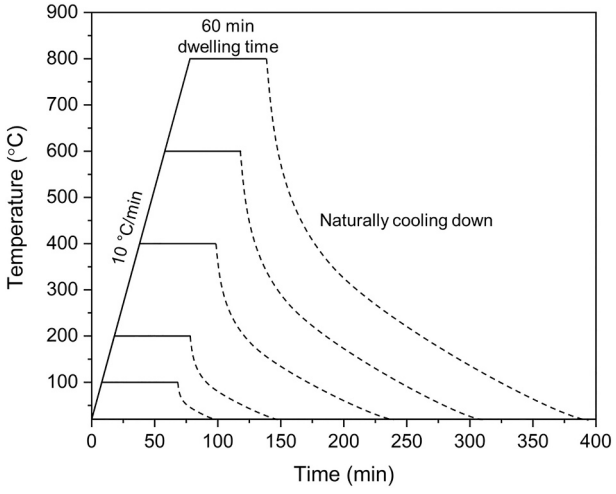

Fig. 3. The schematic diagram of heating curve for different target temperatures.

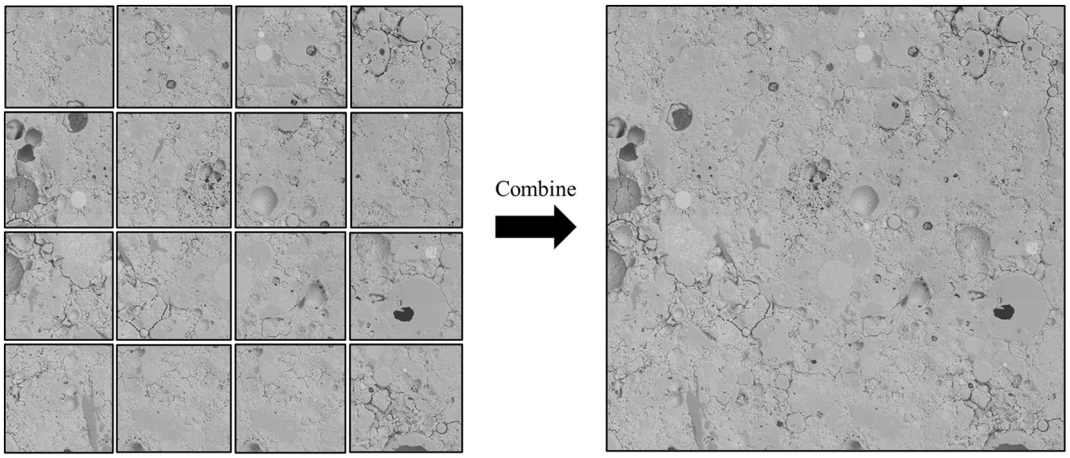

Fig. 4. The image combination for cracking behavior study.

the crack characterization is written in MATLAB R2019a [39]. High resolution 2D images at 2000× magnification (1024 × 1088 pixels) with an area of 134 μm × 134 μm are obtained from polished thin section using SEM, are analyzed. In this process, four steps are involved, and the example of automated procedure for crack mapping is shown in Fig. 5. Firstly, a grayscale method is used to distinguish cracks from background and a binary image is created as shown in Fig. 5b. Secondly, for the calculation of crack length and crack number, the original objects in binary image are skeletonized with a single pixel in thickness, as seen from Fig. 5b-c. Thirdly, to improve the accuracy of calculation, small

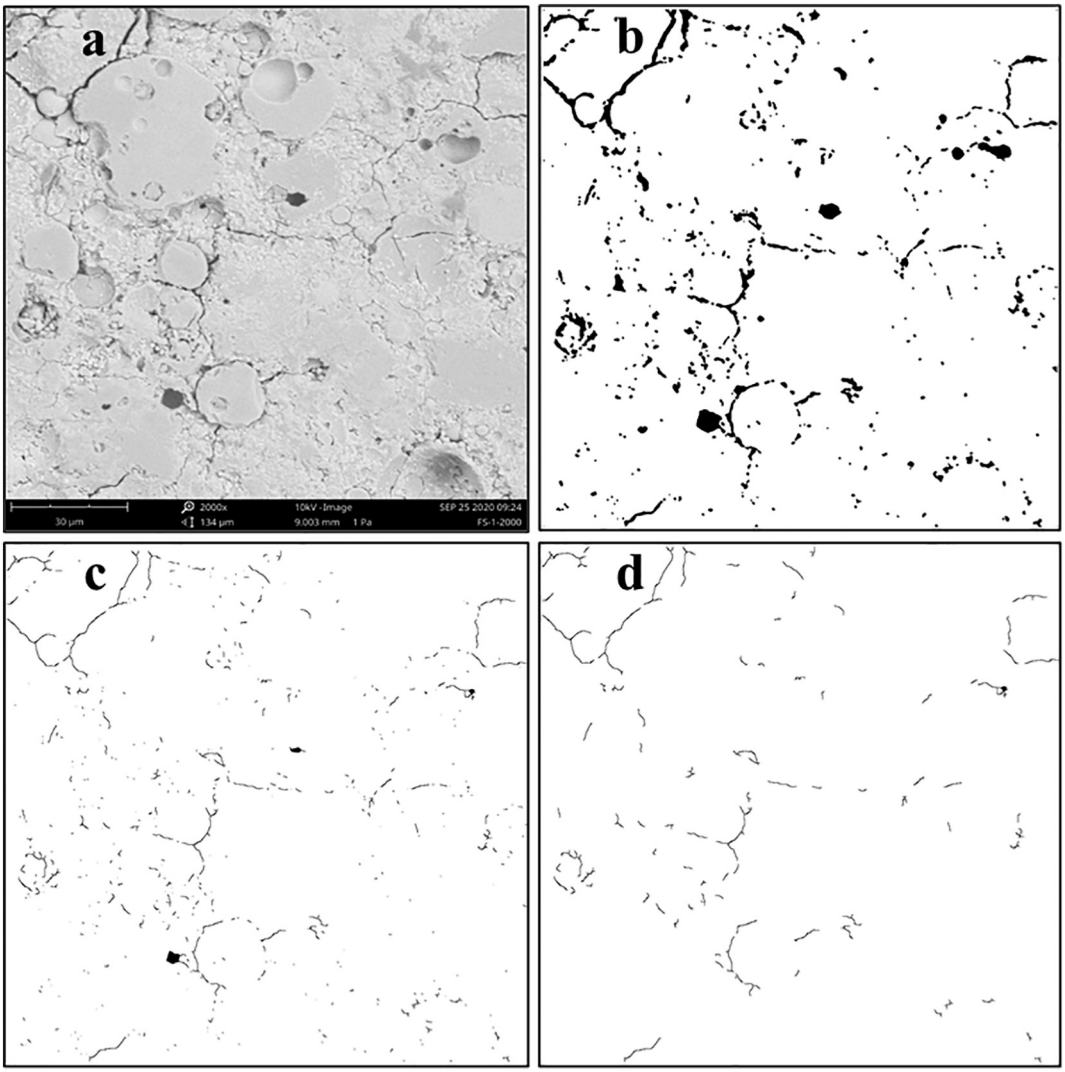

Fig. 5. Processing procedure for crack calculation.

objects induced from pixel noise are removed in Fig. 5d. Fourthly, the microcrack length and microcrack number are automatically calculated based on the identified pixels and structs. The crack density L_A is calculated by,

$$L_A = \frac{L}{A} \tag{1}$$

where L is the cumulative crack length, A is the size of observation area (17,956 μm^2). For each sample, 10 pictures taken in different location are analyzed respectively in order to representatively calculate crack number and cumulative crack length, and the mean value is adopted. Error bars are calculated by the standard deviation from the mean microcrack length, number, and crack density. To validate the proposed automatic procedure, the results are further numerically compared to the UPV results.

2.3.7. Bulk density, skeleton density, open porosity

The bulk density of the obtained samples is calculated by measuring the mass and volume of cubic specimens. The skeleton density is measured using a Micromeritics AccuPyc II 1340 Pycnometer and the test samples are cut into pieces (15 mm × 15 mm × 25 mm) to fit in the testing chamber (diameter of 35 mm). The porosity is calculated according to

$$Porosity\% = \left(1 - \frac{\rho_b}{\rho_s}\right) \times 100\% \tag{2}$$

where ρ_s represents the skeleton density, ρ_b is the bulk density.

2.3.8. Mercury intrusion porosimetry

Mercury intrusion porosimetry (MIP, AutoPore IV 9500, Micromeritics) analysis is performed on the samples before and after subject to different temperatures to measure the pore size distribution and porosity. Before MIP analysis, all the tested samples are cut and sieved to obtain particles with a grain size around 4 mm.

2.3.9. Ultrasonic pulse velocity

The ultrasonic pulse velocity (UPV) is determined according to ASTM C597–16 [40]. The test is performed by a Pundit 200, Proceq (Switzerland). A constant signal of frequency 54 KHz, pulse voltage 50 V is sent from a transducer (diameter of 50 mm) to pass through cubic specimens (100 mm × 100 mm × 100 mm), and the signal is captured by another transducer. This method involves measuring the travel time over a known transmit distance of an ultrasonic wave pulse, and the pulse velocity is calculated by dividing the transmission duration from the thickness of the test specimens,

$$V = \frac{d}{t} \tag{3}$$

where d represents the distance and t is the transit time.

2.3.10. Strength test

The compressive strength is determined according to EN 196–1 [41], and paste samples are tested. The loading rate applied is 2400 N/s and the compressive strength value is recorded as the average of the compressive strength of three specimens.

3. Results

3.1. Chemical transformation

3.1.1. Crystalline phase

Fig. 6 shows the XRD patterns of AAF and AAFS pastes at different temperatures. Before thermal exposure, comparable features are identified in AAF and AAFS, with the main crystalline phases are quartz, mullite, hematite and magnetite, which are similar to raw FA. This indicates that the crystalline phase of AAFS is mainly determined by FA. Moreover, the typical slag related hydrates C-S-H is not observed in this work. This might be because, in a high NaOH concentration and low slag addition system, the Ca^{2+} content is insufficient to form crystalline C-S-H gel but replace Na^+ in geopolymeric gel to form N-(C)-A-S-H hybrid gel [42].

When exposed to elevated temperatures, there is no distinct change identified in AAF and AAFS pastes before 600 °C, indicating that both binders are chemically stable without the formation of new crystalline phases. While a significant change in crystalline phases is detected after exposure to 800 °C. An obvious peak of nepheline ((Na, K)$AlSiO_4$) is noticed at around 34° 2 theta in AAF, which is because of the partial crystallization of N-A-S-H gel [23]. Similarly, nepheline is observed in AAFS, confirming the presence of N-A-S-H in hybrid binder. However, a minor majority of akermanite ($Ca_2MgSi_2O_7$) and gehlenite ($Ca_2Al[AlSiO_7]$) are also detected in AAFS. This observation is highly associated with the addition of slag [43]. The crystalline phases of quartz, mullite, hematite, and magnetite can be found at all test temperatures, which are neither affected by alkali activation nor high-temperature exposure.

3.1.2. FTIR

FTIR test is carried out to study the chemical change under high temperatures. Fig. 7a shows the FTIR spectra of raw FA and GGBS. The main band observed at 870 cm^{-1} in GGBS as well as the band at 1040

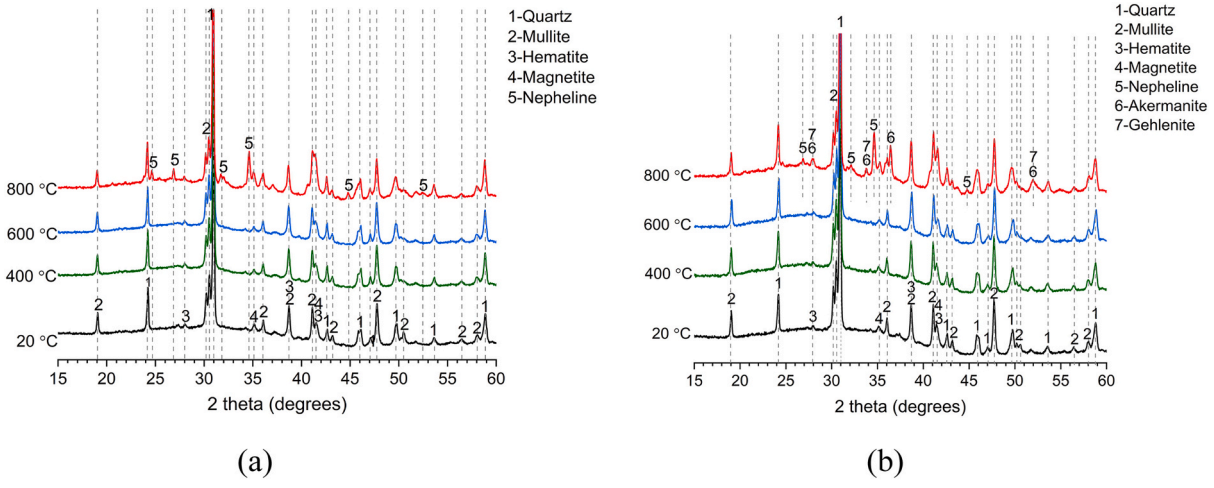

Fig. 6. XRD patterns of different materials (a) AAF and (b) AAFS pastes at different temperatures.

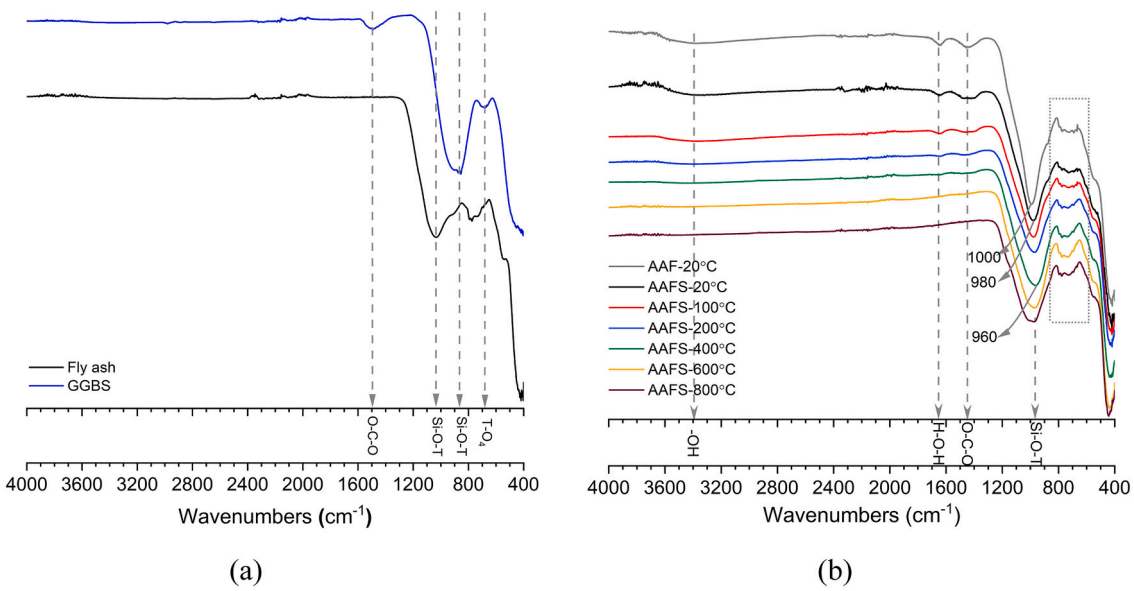

Fig. 7. FTIR spectra (a) solid raw materials and (b) AAF and AAFS pastes before and after elevated temperature exposure.

cm^{-1} in fly ash are both attributed to the asymmetric stretching vibration of Si-O-T bonds, in which T represents Si or Al units. For fly ash, the band in the range of 670–850 cm^{-1} is associated with the stretching vibrations of Si-O-Si in quartz. In GGBS, the vibration band at 1420 cm^{-1} is due to the asymmetric stretching vibration of the O-C-O bonds, indicating the presence of calcite, as also observed in XRD (Fig. 2). And a small absorption band at 670 cm^{-1} is assigned to the asymmetric T-O stretching vibrations.

The infrared spectra of AAF and AAFS paste are shown in Fig. 7b. After alkaline activation, it can be observed that, as compared to raw fly ash, the typical adsorption band of the Si-O-T bridge bond undergoes an obvious shift from 1040 cm^{-1} to 1000 cm^{-1} in AAF, and further shifts to 980 cm^{-1} in AAFS, which indicates the different degree of polymerization. Other chemical bonds observed in AAF and AAFS are identical. A broad absorption band appearing at around 3400 cm^{-1} is associated with the vibration from free water, while the H-O-H bending vibration band at 1640 cm^{-1} is associated with the presence of physically and chemically bond water in the reaction product, which is not identified in the raw materials. As a consequence of thermal treatment, a further shift of the Si-O-T band from 980 cm^{-1} to 960 cm^{-1} is observed in AAFS as the exposure temperature increases from room temperature to 400 °C. It can be related to the increasing temperature favors a further polymerization and a higher degree of calcium contained cross-linking is formed [21]. After exposed from 400 to 800 °C, this peak position keeps constant, but the absorption area becomes broader and wider. This sharp feature is an indicator of the structural disorder in the binder gel induced by elevated temperature [22]. In addition, it should be noted that the absorption band at 3400 cm^{-1} as well as the H-O-H bending vibration band at 1640 cm^{-1} linking to physically and chemically bond water becomes invisible at 600 °C, indicating that the loss of moisture is completed before 600 °C. The vibration band for carbonates from soluble alkali species also disappears between 400 and 600 °C. Moreover, there is no significant change in the quartz band between 670 cm^{-1} - 850 cm^{-1}, which is consistent with the previous XRD results, confirming that quartz phase is quite stable at all test temperatures, and only an alpha-beta transition of quartz occurs at around 600 °C [44].

3.1.3. Thermal analysis

The TG-DTG results of AAFS pastes treated with different temperatures are shown in Fig. 8. The results can reflect the phase change during thermal exposure test since the same heating rate as thermal exposure test is applied. For unheated specimens, the maximum weight loss peak

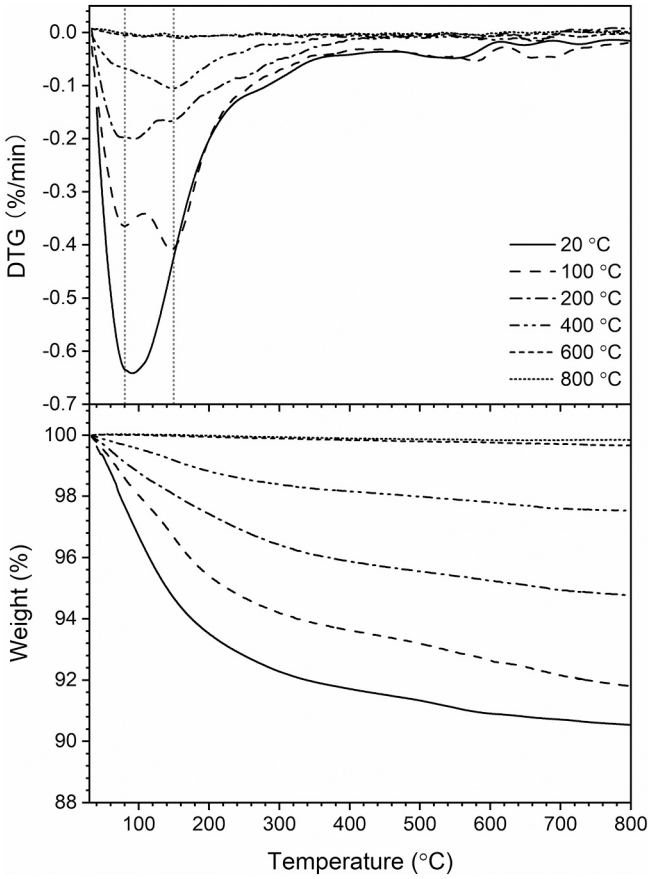

Fig. 8. TG-DTG analysis of AAFS blend.

can be detected at around 100 °C, and this is associated with loss of free water. Furthermore, the weight loss peaks between 480 and 590 °C should be due to the decomposition of calcium carbonates of different crystallinity [45], which agrees with the FTIR results. Some insignificant weight loss peaks after 600 °C might be because of the re-crystallization of hydration products [46]. As for thermal treated samples, it is interesting to note that the 100 °C treated sample shows two peaks between

20 and 200 °C. It suggests that the sharp peak at around 100 °C observed in 20 °C sample should be derived from two peaks. The first peak at around 80 °C is mainly due to the evaporation of free water within the mixture [3], while the second peak observed at around 150 °C can represent the initial dehydration of hydrated aluminosilicate species [30,47]. It is possible that the extensive peak due to the loss of free water overwhelms the endothermic peak of chemically bound water loss from aluminosilicates species, thus showing a combined peak in 20 °C sample. After exposed to 100 °C, free water is partially evaporated, which further weakens the corresponding endothermic peak, and thus two endothermic peaks can be observed at 80 and 150 °C respectively in 100 °C treated sample. Here, it should be mentioned that the mass losses before 200 °C in low temperature treated samples (100 °C, 200 °C, 400 °C) are resulted from the residual physically and chemically bonded water after corresponding thermal treatment, indicating the relatively low exposing temperature might be unable to remove all evaporable water. By comparing the DTG curves of AAFS exposed to different temperatures, the intensity of the first peak keeps decreasing and could not be detected from 400 °C treated sample, which reveals that the free water continues to be released till 400 °C. Moreover, the second peak is not identified as the exposure temperature increases to 600 °C. It suggests that the hydrated aluminosilicate species experiences a slow and lengthy dehydration process from 150 to 600 °C, which is consistent with the FTIR results.

3.2. Structural changes

3.2.1. Qualitative observations

The evolution in appearance of the AAFS before and after exposure to different temperatures is shown in Fig. 9. In Fig. 9a, before exposure to high temperatures, the obtained AAFS paste exhibits a homogeneous appearance without any visible cracks. It can be observed from Fig. 9b-f that the sample morphology changes along with increasing exposure temperature, such as the formation of cracks, the changes in color and texture. Among which, the surface color gradually turns to reddish-brown from room temperature to 800 °C, owing to the oxidation of iron present in fly ash, which is always the case in the fly ash-based system when exposed to high temperature [48]. The crack development under elevated temperature is in accordance with the mass loss observed in TG results. When exposed from 100 to 600 °C, the matrix exhibits a more severe cracking. This is mainly because, as the external temperature increases, moisture within the hybrid binder rapidly migrates to the surface and evaporates, which, in turn, causes surface-cracking and internal damage. Notably, a smooth texture with obviously fewer cracks is detected after 800 °C exposure, which might be attributed to the healing effect caused by viscous sintering reaction. It should be emphasized that the AAFS blends maintain the structural integrity at all tested temperatures.

3.2.2. Skeleton and bulk density

The volume change of geopolymers under elevated temperatures can be reflected by density variation. Among these, the skeleton density variation trend could reflect the change of binder gel structure under high temperatures, while the change in bulk density represents not only the binder gel but also the pore structure transformation. To identify the unique structural change of AAFS geopolymers under elevated temperature, the variation of skeleton density and bulk density of AAFS is compared with AAF as shown in Fig. 10.

In Fig. 10a, it is noted that the initial skeleton density of AAF is higher than that of AAFS, indicating a stronger binder gel formed in AAF. Moreover, an obvious rise of skeleton density is observed in AAF from 20 to 600 °C, following a sharp reduction after 800 °C exposure. In comparison, the skeleton density of AAFS undergoes a slight increase till 200 °C, then stabilizes at around 2.381 g/cm^3 between 200 and 600 °C before a drop at 800 °C. The rise of skeleton density up to 400 °C can be mainly attributed to the further polymerization of the binder as observed in FTIR, which leads to a higher degree of cross-linking. Here, in contrast to the notable densification of AAF skeleton, the insignificant variation of skeleton density in AAFS between 200 and 600 °C might be because a balance between the formation of additional gel and depolymerization of binder gel is reached. After exposure to 800 °C, the reduction of skeleton density in both matrixes could be attributed to two causes. For one thing, as learned in XRD results, porous crystalline phases such as nepheline are detected at 800 °C, which reduces the skeleton density [31]. As a result, more nepheline can be formed in AAF pastes owing to its rich N-A-S-H gel, leading to a more significant

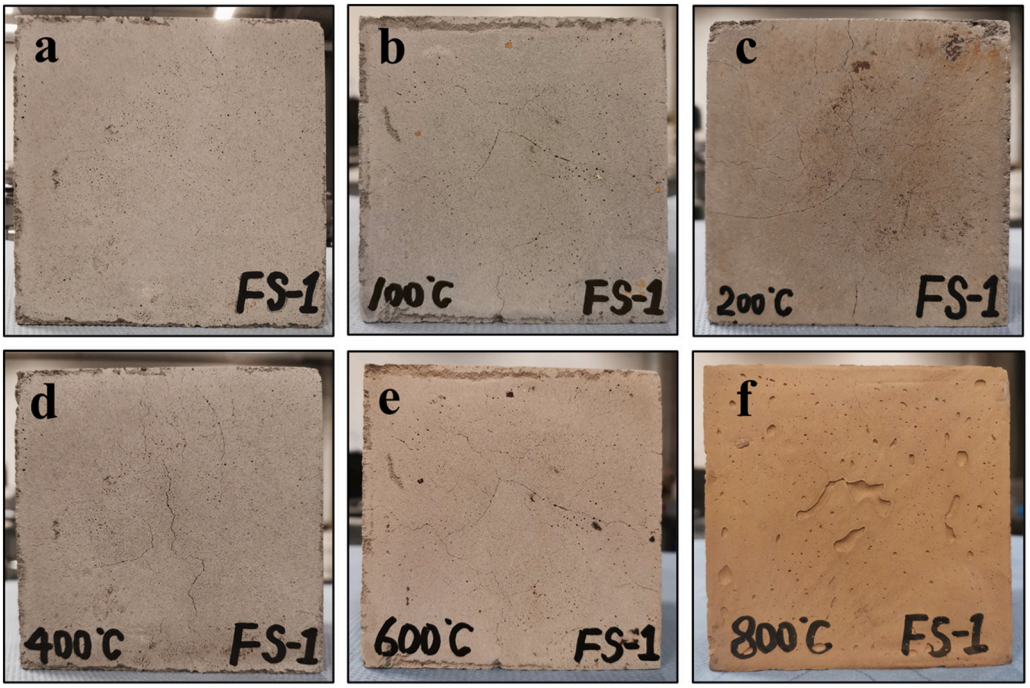

Fig. 9. Visual appearance of AAFS pastes at different temperatures. (a: 20 °C; b: 100 °C; c: 200 °C; d: 400 °C; e: 600 °C; f: 800 °C).

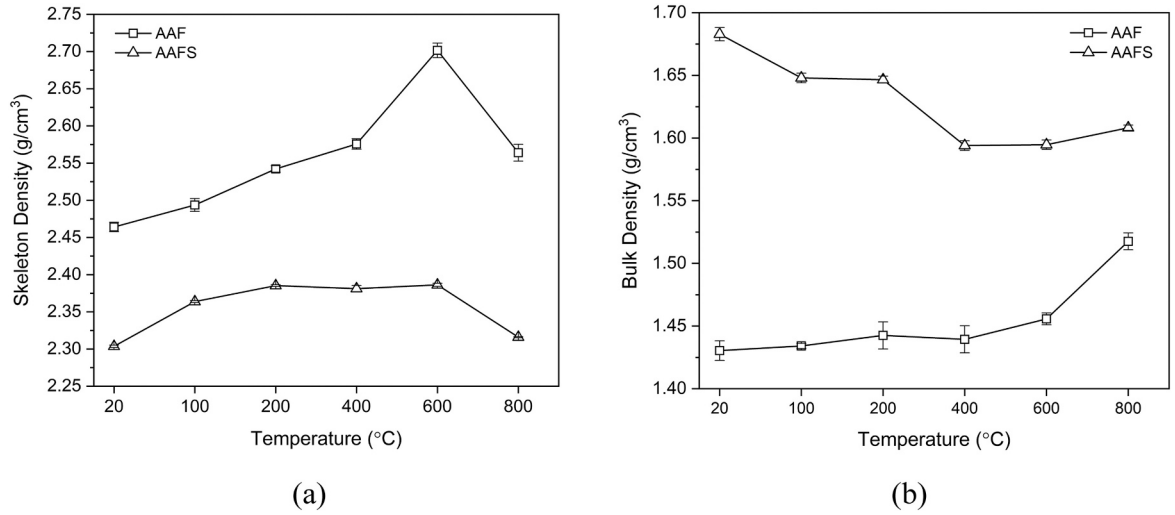

Fig. 10. (a) Skeleton density and (b) bulk density of pastes exposed to different temperatures.

reduction. For another, the sintering reaction might account for the skeleton density reduction, which will be explained in subsequent sections.

As shown in Fig. 10b, the AAFS paste has a much higher bulk density as compared to AAF. When exposed to elevated temperature, the bulk density of AAF almost remains unchanged before 400 °C whereafter largely increases up to 800 °C, while that of AAFS keeps falling before 400 °C, and then a slight increase is detected in the range of 400 to 800 °C. The decrease of bulk density before 400 °C in AAFS is mainly associated with the drastic mass loss as observed in TG, in which the evaporation of free water and chemically bound water leads to crack formation and looser matrix. In contrast, the loose matrix with a lower bulk density in AAF facilitates the water migration, which remains stable under high temperature. After 600 °C, the viscous sintering of unreacted FA leads to the densification of the matrix [3]. Thus, the bulk density increases in both mixtures, and a larger increase is noticed in AAF.

3.2.3. *Pore structure*

Fig. 11 displays the pore size distribution (PSD) in AAF and AAFS pastes at different temperatures observed by MIP. It is known that the intrusion data used in MIP analysis are measured by pore throat size instead of pore radii [49], which only serves as comparative indices for the connectivity and pore capacity [49,50]. Due to the fact that cracking has a strong influence on pore throat size as well as pore connectivity [51], the MIP is capable to reflect the inner structure change including inherent pore structure and the formation of cracks. But, it should be mentioned that, due to the threshold effect during MIP measuring, large pores with small pore throat size might be identified as smaller pores, which results in the test intruded value and porosity relatively lower than the actual value [52].

Clearly, the AAF and AAFS pastes exhibit different PSD at room temperature. The PSD of AAF sample is mostly below 300 nm with the highest peak centered at around 30 nm, and AAFS has the similar PSD range but the pores of 5–10 nm is observed to be the highest fraction. Therefore, it can be deduced that AAFS exhibits a higher degree of reaction since the pore size may reflect the reaction degree, and the well-reacted sample exhibits a higher proportion of gel pores (<10 nm) [53]. In addition, different evolution patterns of PSD are observed between AAF and AAFS under high temperature exposure. The PSD of AAF shows an insignificant change with the majority of pores remains below 300 nm before 600 °C. The pore fraction centered at 15 nm is reduced, and the main pore fraction of 30 nm shifts to 40 nm with a higher fraction at 100 °C and keep decreasing from 100 to 400 °C. In accordance with the skeleton density variation, the reduction of pore fraction can be attributed to the further geopolymerization and contraction of geopolymer gel, while the shift of pore fraction to a larger size should be induced by cracking. The PSD transfers to a wider range at 600 °C and then becomes

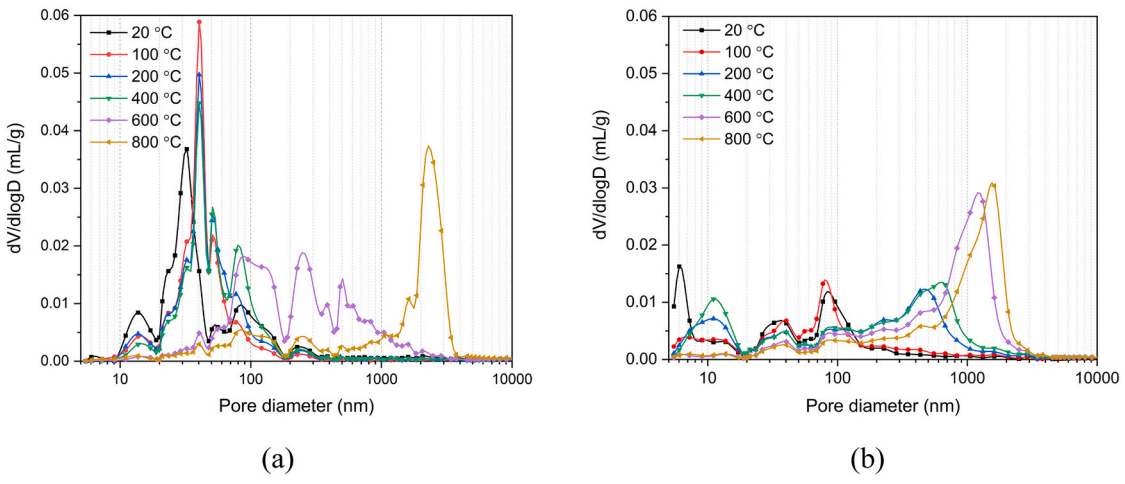

Fig. 11. The pore size distribution of pastes subjected to different temperatures, a) AAF, b) AAFS.

narrower with the main fraction of pore diameter around 2500 nm at 800 °C, which might be because the sintering reaction fills up small pores, but big voids are formed. As compared to AAF, the PSD of AAFS is relatively stable at 100 °C, except the main fraction of pores from 5 nm to 10 nm disappears. However, from 100 to 400 °C, the fraction of pore diameter around 10 nm increases, and the pore fraction between 20 nm and 50 nm shifts to a larger diameter from 200 nm to 1000 nm. According to the density change in Fig. 10, it is possibly due to the dehydration and decomposition of hydrated aluminosilicate species damage the matrix and enlarge the original cracks, contributing to a shift of pore fraction to larger sizes. After exposure to 600 °C, the pore size distribution is narrowed with the main fraction of pore diameter around 1000 nm, and no significant change in the pore distribution occurs at 800 °C.

To further learn the pore structure evolution under elevated temperature, the porosity of AAF and AAFS at different temperatures are compared in Fig. 12. Here, to determine the effect of threshold on MIP results, the intrudable porosity from MIP is further compared with calculated porosity. The tested results are relatively lower than calculated porosity for both pastes. By comparison, obvious discrepancy is noticed in AAFS, especially at 100 °C, indicating that the threshold effect is more predominant in a dense matrix with low porosity. Here, it is likely that the further geopolymerization occurred at 100 °C plays a dominant role in AAFS matrix which narrows the pore throat and largely intensifies the threshold effect, resulting in an underestimate on pore fraction. With increasing exposure temperature, the tested value is getting more approximate to the numerically calculated value in AAFS due to the thermal induced cracking increases the porosity and pore connectivity, hence weakening the threshold effect. In general, there is no significant difference between the porosity from MIP and calculation, and a comparable trend is observed.

As shown in Fig. 12, it is clear that AAFS paste exhibits a lower initial porosity of 23.3% comparing to AAF of 39.5%. From 100 to 600 °C, the porosity of AAFS undergoes an obvious rise from 21.7% to 33.9%, while that of AAF is stabilized between 41.1% and 42.6%. Reduction of porosity is detected in both samples at 800 °C due to sintering reaction, in which a larger reduction of porosity observed in AAF indicates a more drastic viscous sintering occurred in pure FA based geopolymer. In order to identify the thermally induced structural change in different scale, the pore fraction are further divided into three categories: mesopore (2–50 nm), macropore (50–7500 nm), and megapore (>7500 nm) [54]. In AAF, the mesopores keep reducing while the macropore is increased before 400 °C. This is because, on the one hand, the further geopolymerization refines the pore structure and reduces the fraction of mesopores. On the other hand, the contraction of geopolymer gel might transform mesopores to macropores. At 600 °C, the severe shrinkage of binder gel as observed in Fig. 10a remarkably contributes to the transformation of mesopores to macropores. By comparison, a similar reduction of mesopores is noticed in AAFS at 100 °C due to further geopolymerization. While the *meso*pores and macropores are observed to increase since 100 °C, confirming that the dehydration of matrix and decomposition of binder gel take place simultaneously, which not only introduces microcracks but enlarges intrinsic pores or cracks at the same time. After 600 °C, the further degradation of hybrid binder largely increases macropores, resulting in the highest porosity. Accordingly, the thermal-induced pore structure change in AAFS pastes could be divided into 3 stages: i) At 100 °C, the formation of additional gel due to the further geopolymerization densifies the pore structure. ii) between 100 °C and 600 °C, due to the removal of free water and severe decomposition of binder gel further destroy the matrix, the pore interconnection as well as porosity increases continuously. It should be emphasized that before 400 °C, the fraction of pores in all size range increases slowly, while a sharp increase of macropore is observed at 600 °C, indicating that the matrix undergoes a violent deterioration from 400 to 600 °C. iii) upon 600 °C, the viscous sintering starts to dominate the decomposition of binder gel, which densifies the matrix. As a result, the fraction of meso pores largely decreases and a reduction in porosity is observed.

3.3. SEM and EDS analysis

The gel transformation at different temperatures is verified by SEM and EDX analysis in Fig. 13a-h. It should be noted that observable pores around 5–10 μm present in both pastes, which is inconsistent with MIP results. This is likely caused by dropping out of fly ash particles during polishing and/or the threshold effect in MIP measurement.

Before exposure to high temperatures, AAF exhibits a loose matrix, consisting of N-A-S-H gel and abundant unreacted fly ash (Fig. 13a). As for AAFS, a compact matrix with less unreacted fly ash but obvious microcracks is observed in Fig. 13e. Here, the formation of microcracks is mainly attributed to the autogenous and drying shrinkage during curing because of the synergetic effect of factors such as slag addition, w/b ratio, curing condition [55–57]. Meanwhile, due to the dense matrix, slight number of cracks might be induced during drying process before SEM. In contrast to AAF, the matrix of AAFS is dominated by a hybrid N-C-A-S-H gel, which is consistent with previous studies on blended systems with low slag addition [21,58]. In Fig. 13b and f, a coarser texture with additional grains is detected in both samples at 100 °C. These dispersed grains could be due to the further geopolymerization as also noticed in FTIR and MIP results. As the exposure temperature increases to 600 °C, the binder phase of AAF exhibits a good

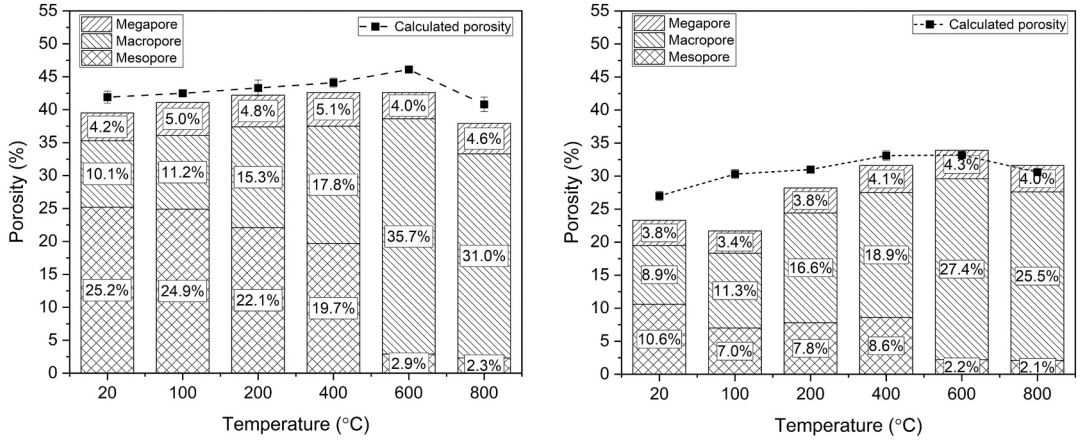

(a) (b)

Fig. 12. The porosity of pastes at different temperatures from MIP, a) AAF, b) AAFS.

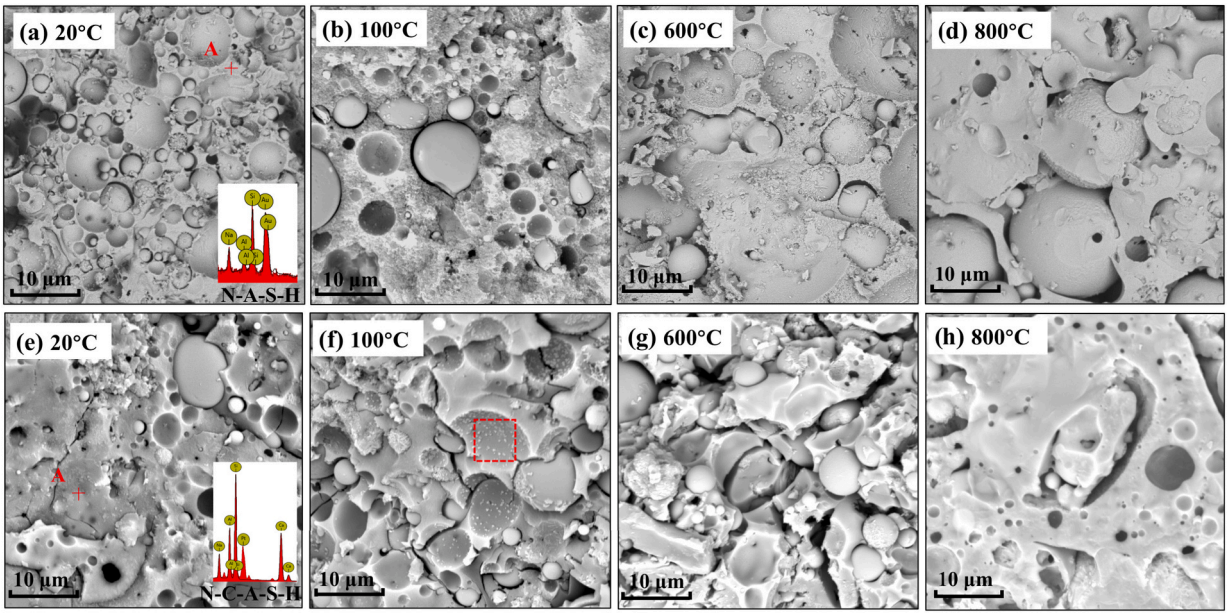

Fig. 13. SEM micrographs with EDX results of samples at different temperatures, AAF: (a), (b), (c), (d); AAFS: (e), (f), (g), (h).

stability except the unreacted fly ash particles begin to combine owing to sintering, while AAFS binder gel experiences an obvious degradation with wider cracks. It can be explained by the drastic depolymerization of hybrid gel up to 600 °C. After exposure to 800 °C, the AAF and AAFS pastes exhibit an identical transformation to smoother texture in Fig. 13d and h. This, on the one hand, can be attributed to the sintering reaction of unreacted fly ash that contributes to a better inner particle bonding [59]. On the other hand, partial melting of aluminosilicate gel might occur at 800 °C within the system rich in sodium [34], which fixes small cracks and voids. Here, the sintering reaction and partial melting results in a large number of closed spherical pores/voids which is indetectable in MIP analysis, accounting for the reduction in skeleton density and porosity at 800 °C.

3.4. Cracking/degradation behavior

The cracks and damage incurred to AAF and AAFS blends prior and subsequent to elevated temperatures are compared in Fig. 14 and Fig. 15. Before elevated temperature exposure, a loose matrix with numerous unreacted FA particles is detected in AAF paste. When exposed to elevated temperatures, regardless minor cracks are observed in AAF at 100 °C due to water evaporation, the binder is overall stable and getting increasingly denser before 400 °C, which can be mainly attributed to further geopolymerization. In accordance with the density variation in Fig. 10, the binder gel shrinks after 400 °C exposure, resulting in the formation of voids and widened interfacial transition zone (ITZ) between the hydration products and unreacted FA particles (See Fig. 14h, j). At the same time, small holes on the surface of these particles are detected, indicating that the sintering reaction of residual FA initiates at around 600 °C. Up to 800 °C, a remarkable transition to smoother structure is observed due to the sintering and partial melting.

In comparison, as shown in Fig. 15a, AAFS initially shows a dense matrix with microcracks occurring in the ITZ. As explained above, microcracks are formed by the shrinkage during curing or drying before SEM analysis. When exposed to 100 °C, it is evident that cracks begin to connect through ITZ, and longer cracks are formed. It is because, in a condensed matrix with low ductility, typical long and thin cracks are induced by the evaporation of free water, thereafter, leading to the propagation of cracks through the weak interface. Meanwhile, in the enlarged micrograph in Fig. 15d, tiny microcracks are less visible after 100 °C exposure. Here, the intrinsic cracks are likely to be filled up by the formation of additional hybrid gel at that temperature. However, compared to AAF, the effect of further geopolymerization is lessened in AAFS after 100 °C. The matrix deteriorates with two different crack growth patterns (long and narrow crack, tiny and widened crack) observed from 200 to 600 °C in Fig. 15e-i. During this process, on the one hand, severer thermal stress is generated within the matrix due to the higher exposure temperature, which lengthens and widens the original cracks. On the other hand, the binder gel is observed to be more disordered with evenly distributed small, widened cracks formed after 200 °C, and getting looser with a coarser texture up to 600 °C in Fig. 15i. This is mainly because the decomposition of hybrid gel that severely impacts the compactness of the matrix, allowing for the aggregation of cracks and the formation of voids, which could explain the enlargement of porosity in the MIP results. After exposure to 800 °C, the matrix exhibits a denser texture without any visible microcracks. The viscous sintering as well as partial melting heal small cracks and fill voids, which is consistent with the rise of bulk density at 800 °C in Fig. 10.

In order to understand the cracking behavior of geopolymers, a quantitative characterization of microcrack based on MATLAB is performed on AAF and AAFS, and the evolution of crack number, cumulative crack length and crack density as a function of elevated temperature are summarized in Table 2.

The AAF is relatively stable with few cracks and low cumulative crack length at the investigated temperatures. Reduction in crack number and cumulative crack length is observed at 200 °C owing to further geopolymerization, then the binder gel shrinkage with enlarged ITZ that gives rise to the crack number and length at 400 °C. By comparison, it is clear that AAF sample shows a much higher crack number than AAFS at the investigated temperatures. The further geopolymerization has a limited effect on against cracking in AAFS, in which the crack number keeps growing from 82 to 281 with an increasing crack growth rate from 100 to 400 °C. Here, the growth of cracks mainly results from the strong inner thermal stress and the decomposition of hybrid gel, and the cracks grow faster as the cumulative thermal stress increases with higher temperature. After 600 °C, the number of cracks largely decreases in both pastes. The reduction of cracks after 600 °C could be explained from two aspects. For one thing, as exposed to a higher temperature, small cracks begin to converge into large cracks due to thermal stress. For another, microcracks are partially healed by the sintering reaction. In addition, as compared to AAF, the cumulative crack length in AAFS sharply increases from 799.2 μm to

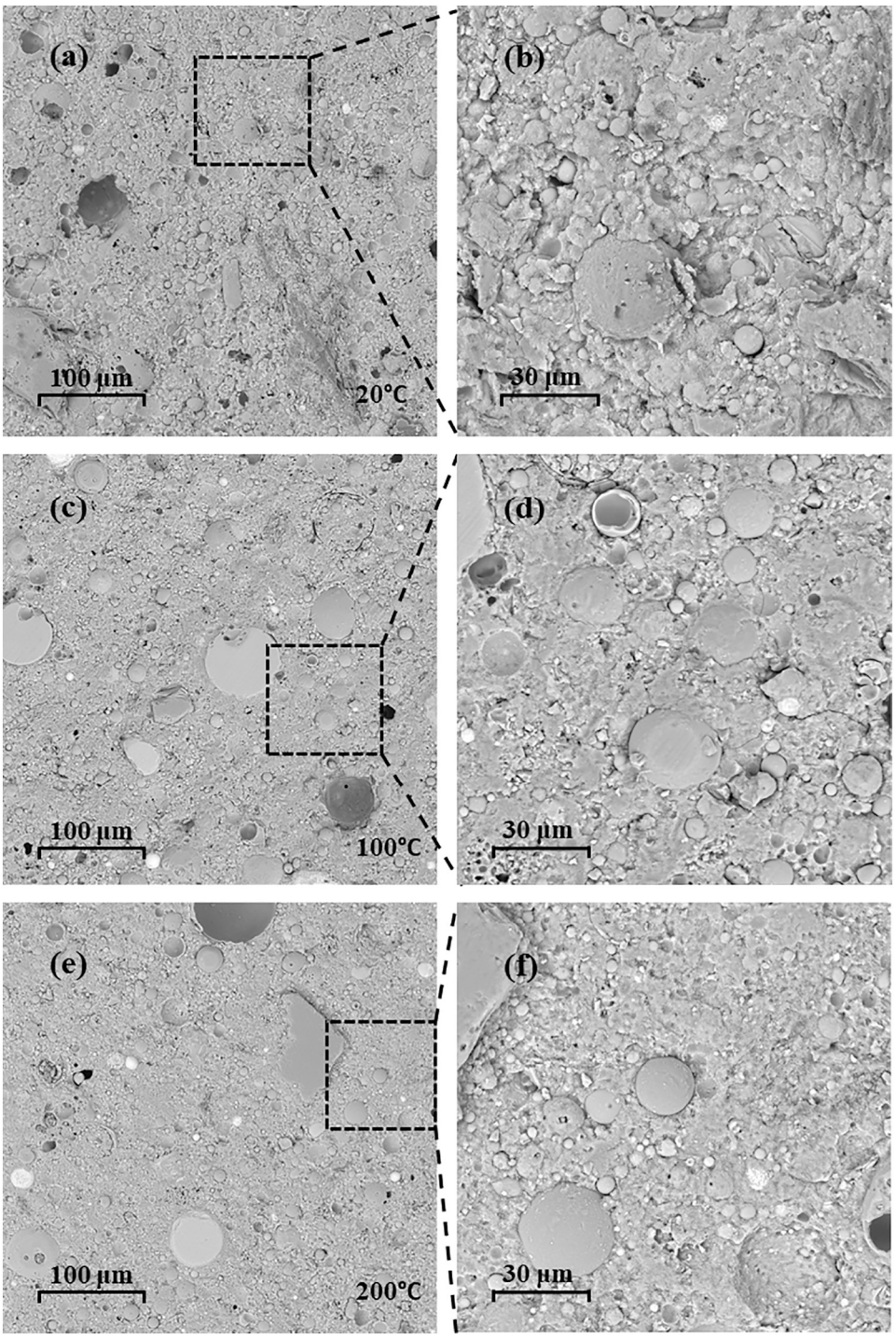

Fig. 14. The microstructure of AAF pastes at different temperatures.

1623.3 μm up to 600 °C, and interestingly, the growth rate of crack length slows down at higher temperature. This is because, in AAFS matrix, the free water evaporation at a lower temperature (before 200 °C) results in the formation of long cracks and largely increases the cumulative crack length. However, as free water is almost evaporated, small cracks are formed owing to the dehydration and decomposition of binder gel, and thus, the increase of cumulative crack length slows down at a higher temperature (after 200 °C), but the crack number grows faster at this stage. The variation of crack density is similar to that of cumulative crack length in both AAF and AAFS samples.

As a non-destructive characterization for assessing the quality of structural concrete, the capability of UPV on estimating the thermal damage of geopolymers is not yet determined. In this work, UPV is performed on AAF and AAFS before and after exposed to elevated temperatures. In Fig. 16a, an opposite trend is observed between AAF and AAFS from 20 to 200 °C, the UPV value of AAF is increased, while that of hybrid AAFS is decreased. After 200 °C, the variation of UPV in AAF and AAFS is similar, which reduces from 200 to 600 °C then increases up to 800 °C. Comparable results are reported by Çelikten et al. [18] that the UPV value of alkali activated slag/fly ash mortar (slag/fly

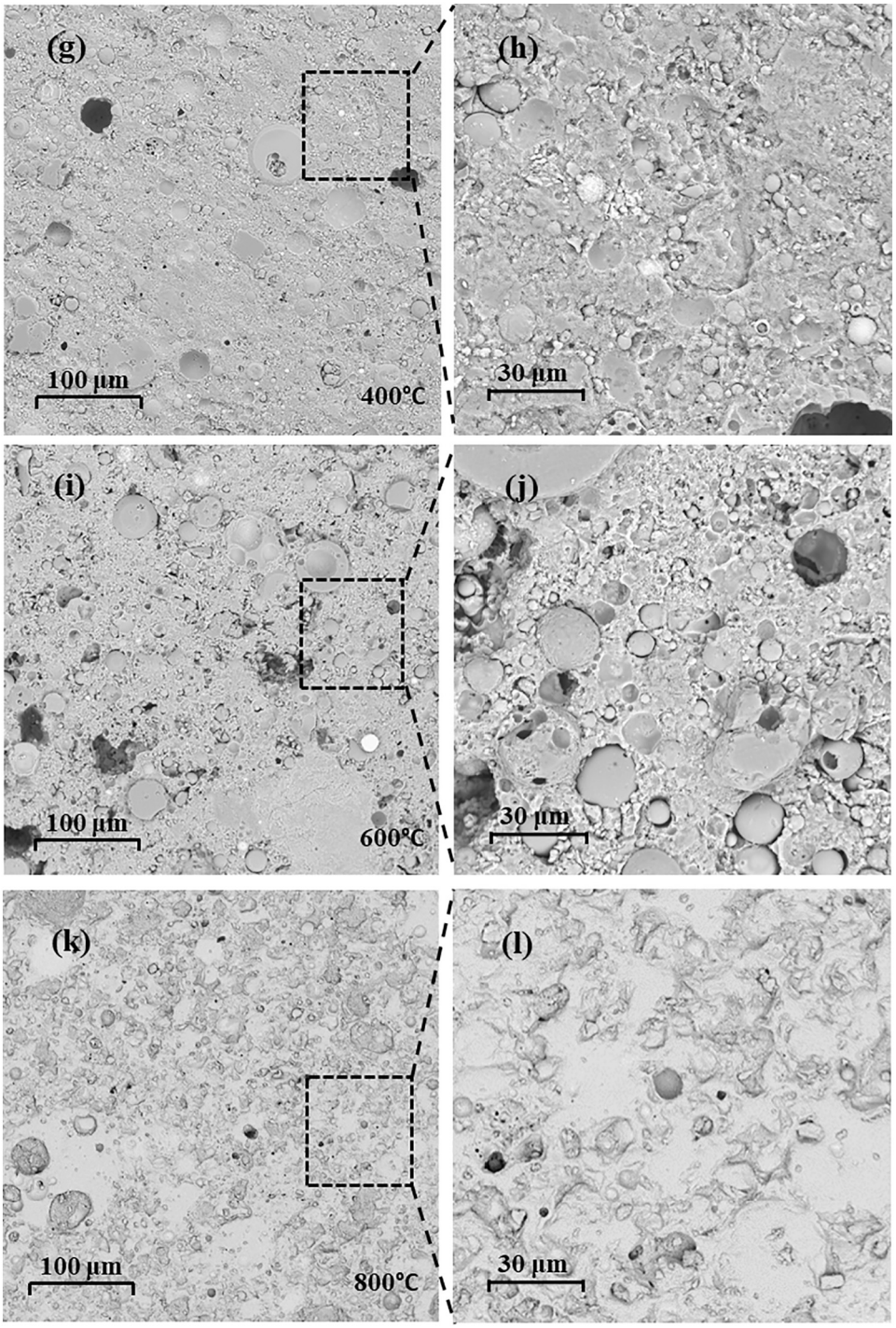

Fig. 14. (*continued*).

ash mass ratio: 50/50) kept reducing with temperature rise to 800 °C. Here, the reduction in UPV value is mainly attributed to the formation of cracks or binder shrinkage, which result in more internal flaws and voids. While the increase of UPV is induced by matrix densification because of further geopolymerization or sintering reaction. It can be deduced that with increasing slag addition, the binder deterioration gradually weakens the positive effect of geopolymeric behaviors such as further geopolymerization or sintering, resulting in a continuous reduction in UPV.

To further set up the correlation between the UPV and crack behavior, the variation of crack density with UPV is plotted in Fig. 16b. Clearly, a linear relationship is seen, and the UPV is negatively related to the crack density in both mixtures. Moreover, it is interesting to note that the correlation between UPV and crack density in AAF and AAFS is fitted into different linear equations with the slope slightly varies. This might be due to the different initial structural properties in AAF and AAFS, such as porosity and density, etc. In general, the result indicates that the UPV can be applied to effectively evaluate the crack evolution or matrix deterioration during high temperature exposure.

3.5. Compressive strength

The strength evolution of AAF and AAFS blends at elevated temperatures are compared in Fig. 17. Before high temperature exposure,

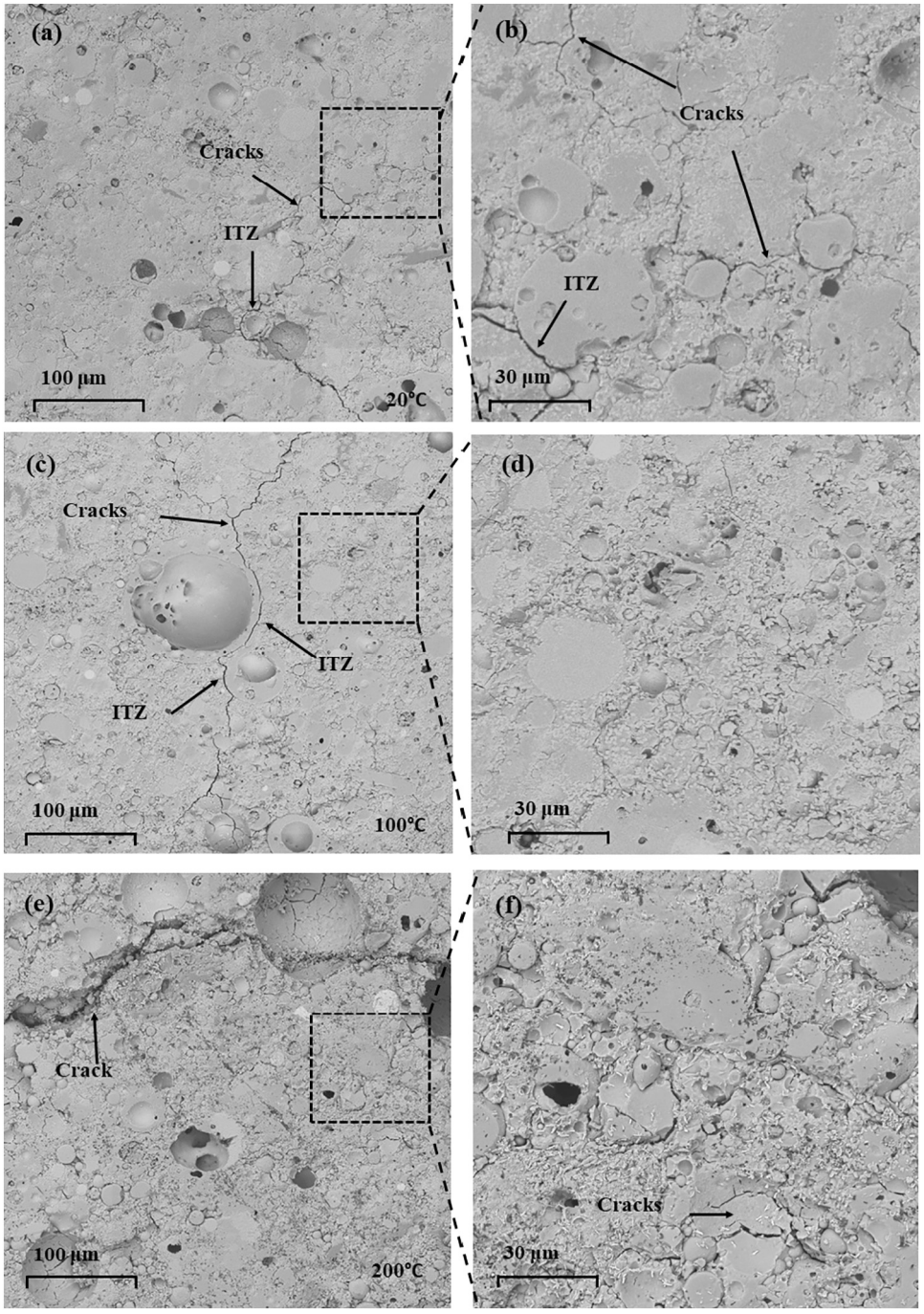

Fig. 15. The microstructure of AAFS pastes at different temperatures.

the AAFS paste exhibits a compressive strength of 47.1 MPa, which is promising as compared to sole fly ash-based pastes of 18.1 MPa. It is because the addition of slag leads to a higher provision of Ca and Si than sole fly ash based system [42,58], and thus, more hydration products are formed in hybrid system. When exposed to elevated temperatures, the compressive strength of AAF shows a sharp rise before 200 °C, and then largely maintains the strength gain effect from 200 to 800 °C with a 150.3% improvement recorded after 800 °C exposure, which is consistent with Kong et al. [35]. In terms of AAFS, the compressive strength slightly increases at 100 °C, then continuously drops as the exposure temperature increases from 100 to 600 °C, reaching the minimum compressive strength of 26.9 MPa at 600 °C. After exposure to 800 °C, a slight increase in residual strength is observed.

At a low temperature exposure, as learned from the corresponding MIP and density results, the further geopolymerization refines the pore structure and strengthens the skeleton, which has a positive effect on the compressive strength. However, when compared to AAF, the higher degree of activation in AAFS in turn hinders the positive effect of further geopolymerization, which only exhibits a slight strength gain up to 100 °C. At intermediate temperatures (100–600 °C), different from the AAF that exhibits a good binder stability, a severer decomposition occurred in AAFS hybrid binder as shown in Fig. 13 and Fig. 15. The increasingly crack formation in different scale could be the main reason for the strength deterioration in AAFS. At 800 °C, as a result of viscous

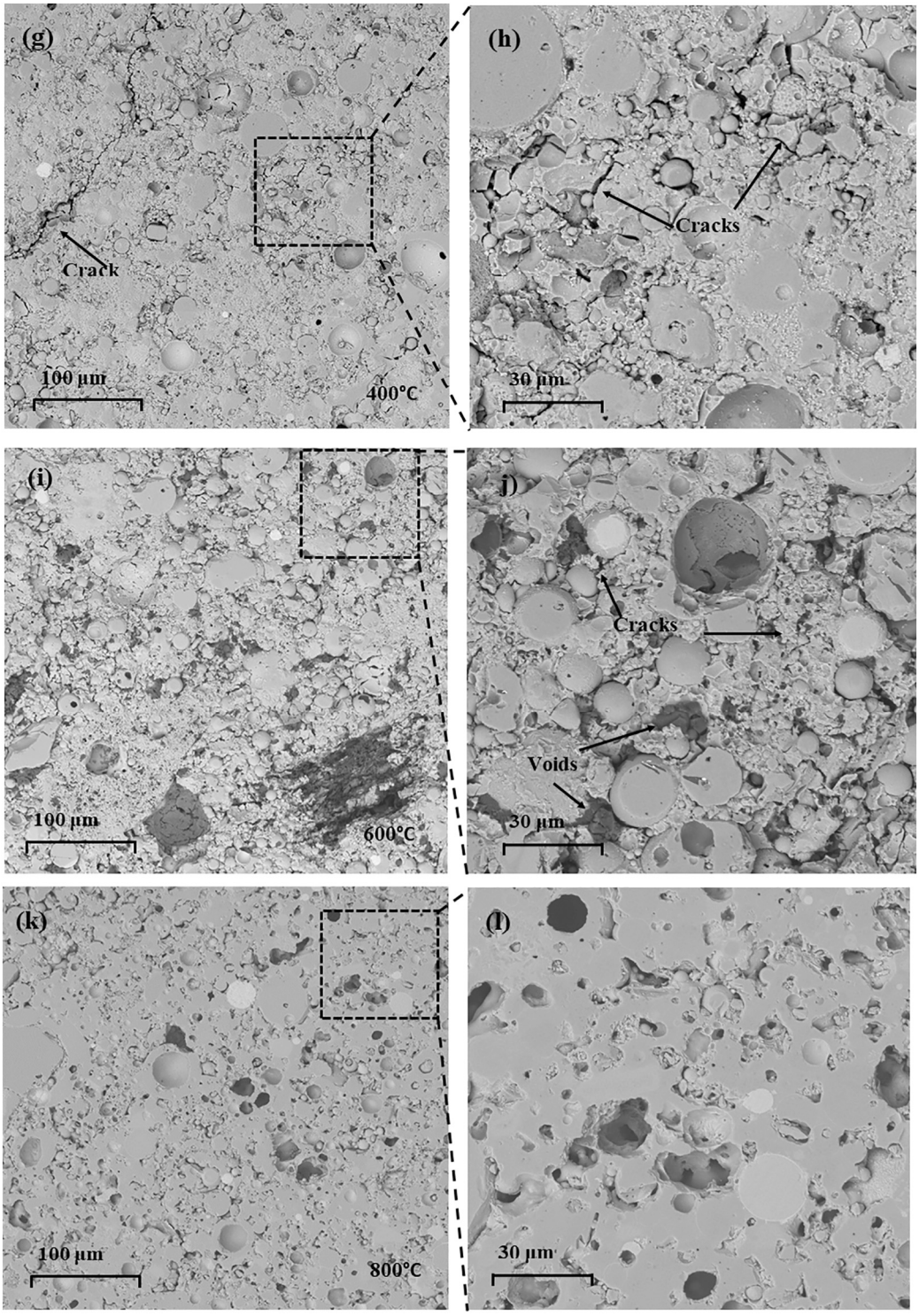

Fig. 15. (*continued*).

sintering, a denser matrix with a stronger ceramic bond is obtained, contributing to a higher compressive strength in both matrixes. Here, the insignificant strength gain in AAFS compared to AAF might be attributed to more drastic crystallization occurs in AAFS at 800 °C as learned in XRD.

4. Discussion

4.1. Degradation mechanisms at high temperatures

As exposed to elevated temperature, AAMs experience a series of chemical transformation and physical change at the same time, which have a synergetic influence on its mechanical strength. It is reported that two competing mechanisms, namely, matrix densification and crack formation, determine the residual strengths of sole fly ash based system

Table 2
The observed crack number, crack length and the calculated value of crack length per unit area in AAF and AAFS under different temperature exposure.

Temperature (°C)	Number of cracks	St dev	Cumulative crack length (μm)	St dev	Crack density (μm/μm^2)	St dev
AAF						
20	32	2	165.6	24.1	0.009	0.001
100	37	3	253.1	36.0	0.014	0.002
200	13	2	117.7	14.8	0.006	0.001
400	39	2	425.4	24.8	0.023	0.001
600	40	2	467.9	50.4	0.026	0.003
800	19	2	249.0	17.6	0.013	0.001
AAFS						
20	82	3	775.9	40.7	0.043	0.002
100	95	28	1098.5	66.0	0.061	0.003
200	164	29	1432.3	76.5	0.080	0.004
400	281	51	1637.7	129.3	0.092	0.007
600	103	14	1773.3	82.7	0.099	0.004
800	71	12	895.3	92.1	0.050	0.005

on exposure to elevated temperatures [22,23]. However, in terms of AAFS hybrid system, the mechanism of strength evolution under high temperature is more complicated since the AAFS blends exhibit a thermal behavior that is influenced not only by FA but also by GGBS [24]. In order to clarify the fundamental role of slag in the high temperature performance of geopolymers, the typical physicochemical transformation and the related competing influence on thermal behavior of AAF and AAFS blends is compared. The conceptual models of AAF and AAFS are proposed in Fig. 18 to explain the degradation mechanism of AAFS blends under elevated temperatures.

Before exposed to higher temperatures, the AAF sample exhibits a porous structure with abundant unreacted fly ash particles and residual water. By comparison, a dense matrix with low porosity, fewer unreacted fly ash but obvious microcracks are observed in AAFS blends. This is mainly attributed to the addition of slag largely promotes the activation process, leading to a compact matrix with a relatively low ductility.

When exposed to 100 °C, with increasing inner thermal stress, the porous structure of AAF facilitates the release of water and in consequence, the matrix is largely retained with minor microcracks. In contrast, due to its dense structure with lower pore connectivity, the existing microcracks in AAFS grow longer and wider, and independent cracks begin to connect through the ITZ as observed in SEM (Fig. 15a-d). On the other hand, the increased temperature favors the further geopolymerization both in AAF and AAFS, which is confirmed by FTIR and density. It is believed that the further geopolymerization plays a key role in geopolymeric matrix to avoid spalling as always experienced by OPC binders under elevated temperature. For one thing, the further

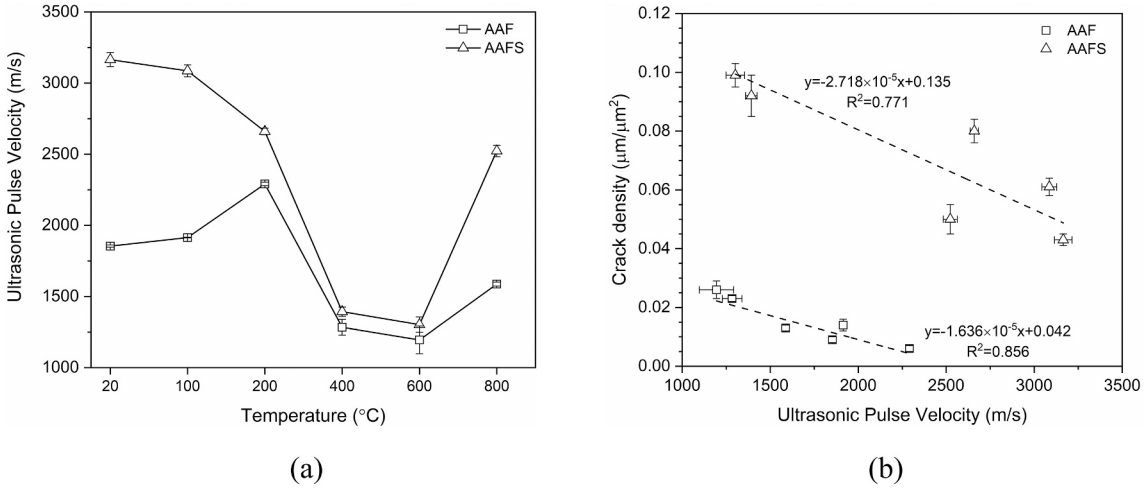

Fig. 16. The relation of crack density and ultrasonic pulse velocity of geopolymers under high temperatures.

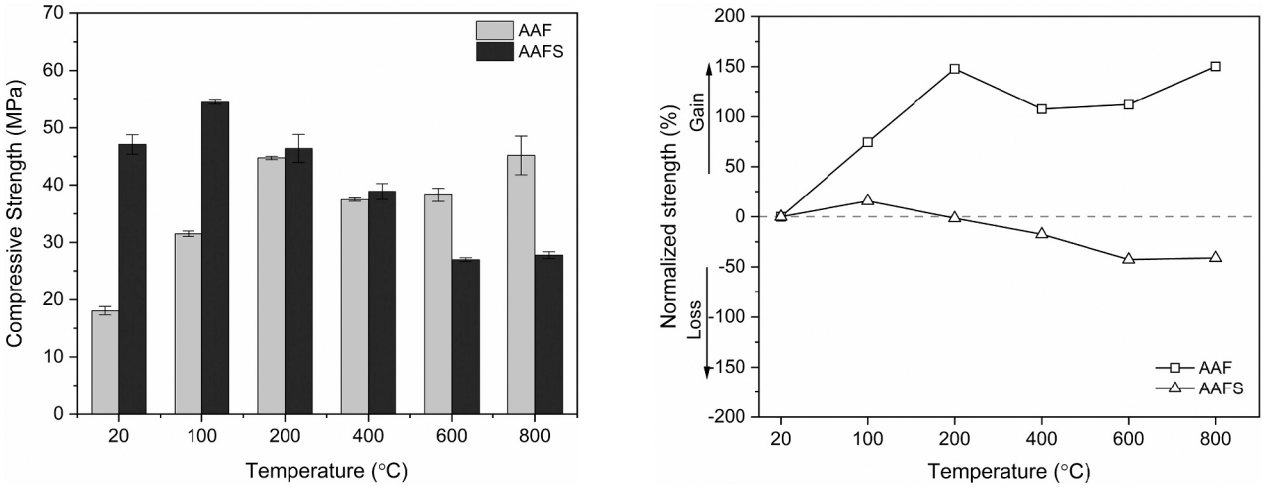

Fig. 17. Compressive strength (a) and normalized strength (b) of AAF and AAFS at different temperatures.

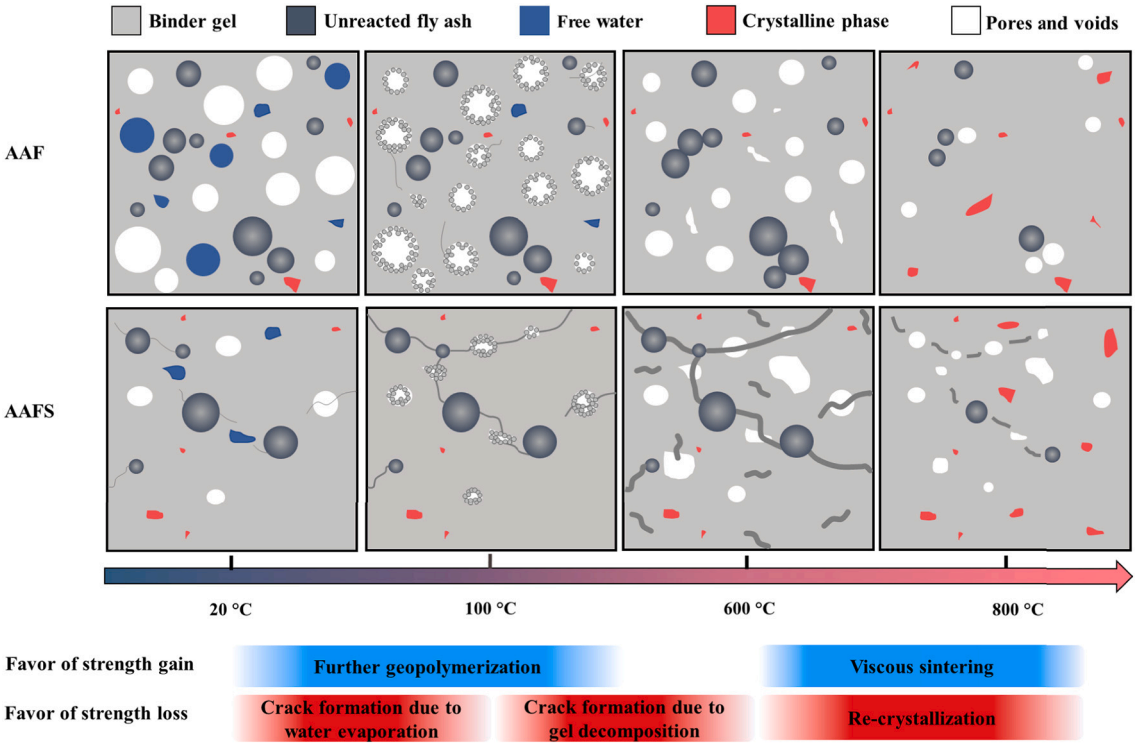

Fig. 18. The conceptual model of the degradation mechanism of AAF and AAFS blends under elevated temperatures.

geopolymerization consumes part of free water, and thus reduces the inner thermal stress to some extent. For another, the further formation of geopolymer gel would fill in the existing cracks, pores or voids, as noted by a reduction in porosity in Fig. 12, thereafter strengthening the matrix. Thus, the further geopolymerization at this temperature compensates for the crack formation induced by free water evaporation. As a result, a strength gain is observed.

In the exposure temperature range between 100 and 600 °C, the geopolymeric binder of AAF still exhibits a good stability and the further geopolymerization keeps playing a predominant role on AAF up to 400 °C. Moreover, the binder phase is detected to rearrange to form macropores due to the binder shrinkage and sintering at 600 °C, but no decomposition of the binder gel is observed. In terms of AAFS, the dehydration and decomposition of hybrid gel shows a dominating effect on the matrix. This is because, with the addition of slag, the sodium in N-A-S-H gel can be substituted by calcium to form hybrid N-C-A-S-H gel, thus decreasing its thermal stability [21]. During this period, on the one hand, moisture within the matrix is completely evaporated along with more severe inner thermal stress, which further widens and prolongs the preexisting cracks (Fig. 15e-j). On the other hand, numerous evenly distributed tiny and widened cracks are formed because of the depolymerization of hybrid gel. The number of cracks rapidly increases during this stage, which brings more micro defects into the AAFS matrix. Big voids are also formed because of the decomposition of binder. These mechanisms give rise to the increase in macropore and megapore fraction as well as the pore interconnection, as evidenced by the MIP results. Consequently, the AAFS blends undergo a drastic strength loss in this temperature range. It reveals that the formation of cracks is the main cause that induces the strength deterioration of AAFS under elevated temperature.

From 600 to 800 °C, the mechanisms of re-crystallization and viscous sintering take place simultaneously in AAF and AAFS. New crystalline phases, such as nepheline, akermanite, gehlenite, appear according to the XRD in Fig. 6. It should be noted that the newly formed porous crystalline phases, such as nepheline, can adversely affects the compactness, leading to a weakened gel skeleton as evidenced by the large decrease in skeleton density in Fig. 10. At the same time, the viscous sintering consumes remaining fly ash to fill small pores and tiny cracks, resulting in an obvious transformation from rough texture to smooth texture. However, as compared to AAF, a portion of big voids and cracks is remained in AAFS due to the drastic matrix deterioration (see Fig. 15k, l). A reduction in porosity from MIP results further proves this transformation. Ultimately, the viscous sintering diminishes the adverse impact of crack formation as well as re-crystallization, and the mechanical strength is retained.

In overall, it should be mentioned that the proposed degradation model and mechanism for AAFS is only valid for low slag contained geopolymer (or N-C-A-S-H gel dominated) system. The thermal degradation behavior may vary with higher slag addition since increasing slag addition could alter the resulted phase composition and microstructure, which deserves further investigation.

4.2. The relationship between cracking behavior and mechanical strength deterioration

As exposed to high temperature, the mechanical property of geopolymers is mainly influenced by thermal induced physicochemical changes. Different from the sole FA based geopolymer that exhibits a good structural stability under elevated temperature exposure, it is notable that AAFS blends inevitably undergo a drastic matrix cracking. As learned from this work, such a discrepancy can be explained from two aspects. From the perspective of microstructure, the hybrid AAFS geopolymers exhibit a denser matrix with higher initial strength but lower ductility as compared to AAF pastes (See Fig. 10 and Fig. 17). During high temperature exposure, higher thermal stress can arise from water evaporation due to the compact structure. Meanwhile, the brittleness of the matrix weakens its compatibility for thermal stress during high temperature exposure, which further aggravates the thermal damage (Table 2). From the point view of binder gel, owing to the slag addition as a source of calcium, the thermal stability of AAFS hybrid gel (N-C-A-S-H gel) is negatively impacted by the Na/Ca exchange. As evidenced by the crack characterization, small cracks grow rapidly at high

temperatures because of the decomposition of hybrid gel, which introduces more defects into the matrix.

As reported in previous works on AAMs [18,30,47,60], it is believed that under elevated temperature, the growth of crack number and size is always accompanied with mechanical strength deterioration. Nevertheless, in the geopolymer system as learned in this study, a more complex relationship between crack behavior and mechanical strength evolution is observed.

The variation of crack density and compressive strength at different temperatures in AAF and AAFS are depicted in Fig. 19. Before 100 °C, the crack density and compressive strength show a positive correlation in AAF and AAFS, the compressive strength increases despite the crack density rises with higher temperatures. While after 100 °C, a negative relationship between the compressive strength and the crack density is observed in both mixtures. Among which, the increase of crack density accompanies with strength deterioration, and the reduction of crack density is associated with strength gain. The observed erratic variation is because in geopolymer system, the mechanical property is not only influenced by cracking behavior but also chemical transformation.

As for AAF, owing to the further geopolymerization, the crack propagation is inapparent at a low temperature, and the crack density is further decreased at 200 °C along with a continuous strength gain. When it comes to AAFS, it is clear that the effect of further geopolymerization is lessened, which could not prevent the increase of crack number and length with exposure temperature. Nevertheless, the further formation of geopolymer gel contributes to a higher degree of cross linking, in that case, strengthening the matrix as well as avoiding spalling during such a violent cracking process. With the exposure temperature keeps increasing, the cracking behavior starts to have a direct influence on the mechanical property of AAFS as the decline of further geopolymerization, which brings more flaws and voids to the matrix and results in a mechanical degradation. In order to hinder/postpone the adverse impact of thermal induced cracking and improve the thermal performance of hybrid geopolymers, effort can be made to enhance the effect of further geopolymerization by tailoring the molecular silicate modulus or water content.

5. Conclusions

This paper aims to understand the underlying mechanism of the mechanical evolution of hybrid geopolymeric binder when exposed to elevated temperatures (up to 800 °C). With a pure fly ash based geopolymer (AAF) as the reference, the synergetic influence of physicochemical transformation on thermal degradation of alkali-activated FA/GGBS (AAFS) blends is revealed by investigating the physicochemical properties such as the stability of crystalline phase and binder gel, skeleton and bulk density, pore structure, cracking behavior and mechanical strength at different temperatures. The following conclusions can be drawn:

(1) AAFS undergoes a severer thermal deterioration as compared to AAF. The hybrid geopolymer has a denser matrix with high initial strength but lower ductility that creates a high thermal stress during the water vapor evaporation. The brittleness of the matrix weakens its compatibility for thermal stress, which further aggravates the thermal damage. Moreover, the thermal stability of geopolymeric gel is negatively impacted by the slag addition, and small cracks grow rapidly at high temperatures because of the decomposition of hybrid gel.

(2) Two different cracking patterns are detected in the AAFS hybrid matrix under elevated temperatures: a) Long and narrow cracks are formed through the interfacial transition zone (ITZ) because of the inner thermal stress induced by the release of free water. b) Evenly distributed and widened cracks result from the dehydration and decomposition of hybrid gel under elevated temperatures. Among these, long, narrow cracks are observed in the early stage, leading to a rapid increase in the cumulative crack length. While a robust growth of widened cracks is observed in the later stage that largely increases the crack number and brings more defects to the matrix.

(3) Within the investigated temperature region, the crack number, cumulative crack length and crack density keep growing in AAFS until the viscous sintering takes place. The crack density exhibits a linear relationship with UPV, which indicates that the UPV is capable of estimating the thermal damage or crack evolution of geopolymers under elevated temperatures. The crack density and compressive strength are not always negatively related as a positive correlation between the two is observed before 100 °C. It is because the thermal-mechanical property of AAFS is not only influenced by cracking but also chemical transformation. At a low temperature, the further formation of geopolymer gel could compensate for the thermally induced cracks and result in a strength gain.

(4) As compared to AAF, the effect of geopolymeric behaviors such as further geopolymerization and viscous sintering is lessened in AAFS. The further geopolymerization in AAFS consumes part of free water and strengthens the gel skeleton, which largely contributes to the matrix for avoiding spalling as violent water evaporation occurs before 200 °C. From 200 to 600 °C, the development of cracks due to the severe dehydration and decomposition of hybrid gel gradually dominates the further geopolymerization, accounting for the main inducer of strength

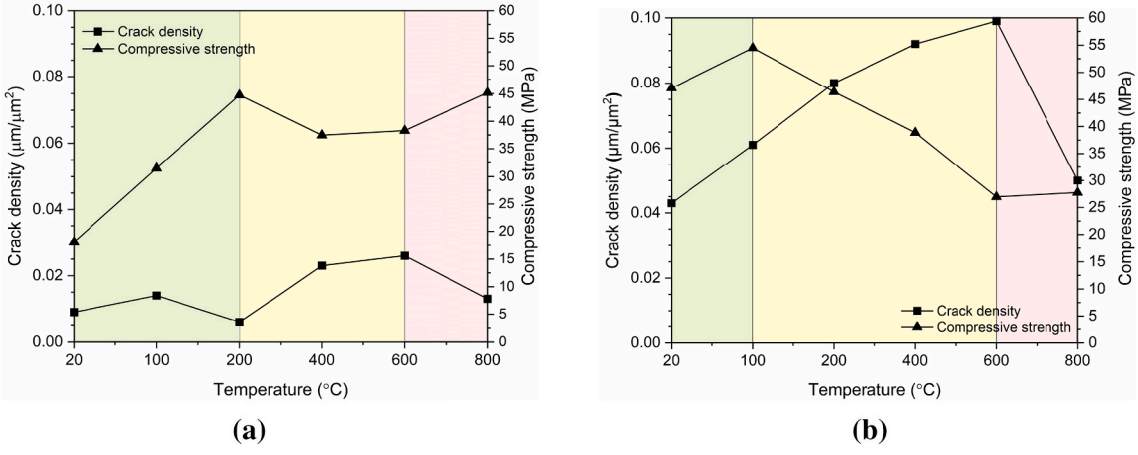

Fig. 19. Comparison of crack density and compressive strength under different temperatures, (a) AAF, (b) AAFS.

deterioration. After 600 °C, the sintering reaction not only partially heals the micro/*meso* pores/cracks but also diminishes the adverse impact of re-crystallization on the gel skeleton, thus the mechanical strength is retained.

CRediT authorship contribution statement

Y. Luo: Methodology, Investigation, Data curation, Formal analysis, Validation, Writing – original draft. **S.H. Li:** Investigation, Writing – review & editing. **K.M. Klima:** Investigation, Writing – review & editing. **H.J.H. Brouwers:** Funding acquisition, Supervision, Writing – review & editing. **Qingliang Yu:** Conceptualization, Supervision, Funding acquisition, Project administration, Writing – review & editing.

Declaration of competing interest

The authors declare that they have no known competing financial interests or personal relationships that could have appeared to influence the work reported in this paper.

Acknowledgements

This research is supported by China Scholarship Council (No. 201906370011) and the department of the Built Environment at Eindhoven University of Technology. Special thanks are given to Mr. W.T. Zhuang at Wuhan University (China) for his help with MIP measurements.

References

[1] A. Fernández-Jiménez, A. Palomo, J.Y. Pastor, A. Martín, New cementitious materials based on alkali-activated Fly ash: performance at high temperatures, J. Am. Ceram. Soc. 91 (2008) 3308–3314, https://doi.org/10.1111/j.1551-2916.2008.02625.x.
[2] I.H. Aziz, M.M.Al Bakri Abdullah, H.C. Yong, L.Y. Ming, K. Hussin, A. Surleva, E. A. Azimi, Manufacturing parameters influencing fire resistance of geopolymers: a review, Proc. Inst. Mech. Eng. Part J. Mater. Des. Appl. 233 (2019) 721–733, https://doi.org/10.1177/1464420716668203.
[3] D.L.Y. Kong, J.G. Sanjayan, K. Sagoe-Crentsil, Comparative performance of geopolymers made with metakaolin and fly ash after exposure to elevated temperatures, Cem. Concr. Res. 37 (2007) 1583–1589, https://doi.org/10.1016/j.cemconres.2007.08.021.
[4] J.L. Provis, Geopolymers and other alkali activated materials: why, how, and what? Mater. Struct. 47 (2014) 11–25, https://doi.org/10.1617/s11527-013-0211-5.
[5] T. Luukkonen, Z. Abdollahnejad, J. Yliniemi, P. Kinnunen, M. Illikainen, One-part alkali-activated materials: a review, Cem. Concr. Res. 103 (2018) 21–34, https://doi.org/10.1016/j.cemconres.2017.10.001.
[6] J. Davidovits, Geopolymers and geopolymeric materials, J. Therm. Anal. 35 (1989) 429–441, https://doi.org/10.1007/BF01904446.
[7] C. Büchler, Fire safety in industrial buildings and nuclear power plants with air-filters made of geopolymer composite, Second Int. Conf. Geopolym. (1999) 181–188.
[8] T.W. Cheng, J.P. Chiu, Fire-resistant geopolymer produced by granulated blast furnace slag, Miner. Eng. 16 (2003) 205–210, https://doi.org/10.1016/S0892-6875(03)00008-6.
[9] A. Buchwald, M. Hohmann, Ch. Kaps, H. Bettzieche, J.-Th. Kühnert, Stabilised foam clay material with high performance thermal insulation properties, CFI Ceram. Forum Int. 81 (2004) E39–E42.
[10] W.D.A. Rickard, A. Van Riessen, Performance of solid and cellular structured fly ash geopolymers exposed to a simulated fire, Cem. Concr. Compos. 48 (2014) 75–82, https://doi.org/10.1016/j.cemconcomp.2013.09.002.
[11] J.I.E. García, K. Campos-Venegas, A. Gorokhovsky, A. Fernández, Cementitious composites of pulverised fuel ash and blast furnace slag activated by sodium silicate: effect of Na2O concentration and modulus, Adv. Appl. Ceram. 105 (2006) 201–208, https://doi.org/10.1179/174367606X120151.
[12] X. Gao, Q.L. Yu, H.J.H. Brouwers, Reaction kinetics, gel character and strength of ambient temperature cured alkali activated slag–fly ash blends, Constr. Build. Mater. 80 (2015) 105–115, https://doi.org/10.1016/j.conbuildmat.2015.01.065.
[13] S. Samantasinghar, S. Singh, Effects of curing environment on strength and microstructure of alkali-activated fly ash-slag binder, Constr. Build. Mater. 235 (2020), 117481, https://doi.org/10.1016/j.conbuildmat.2019.117481.
[14] A. Rafeet, R. Vinai, M. Soutsos, W. Sha, Effects of slag substitution on physical and mechanical properties of fly ash-based alkali activated binders (AABs), Cem. Concr. Res. 122 (2019) 118–135, https://doi.org/10.1016/j.cemconres.2019.05.003.
[15] I. Ismail, S.A. Bernal, J.L. Provis, R.San Nicolas, S. Hamdan, J.S.J. van Deventer, Modification of phase evolution in alkali-activated blast furnace slag by the incorporation of fly ash, Cem. Concr. Compos. 45 (2014) 125–135, https://doi.org/10.1016/j.cemconcomp.2013.09.006.
[16] X. Gao, Q.L. Yu, H.J.H. Brouwers, Apply 29Si, 27Al MAS NMR and selective dissolution in identifying the reaction degree of alkali activated slag-fly ash composites, Ceram. Int. 43 (2017) 12408–12419, https://doi.org/10.1016/j.ceramint.2017.06.108.
[17] H. Ye, A. Radlińska, Fly ash-slag interaction during alkaline activation: influence of activators on phase assemblage and microstructure formation, Constr. Build. Mater. 122 (2016) 594–606, https://doi.org/10.1016/j.conbuildmat.2016.06.099.
[18] S. Çelikten, M. Sarıdemir, İ. Özgür Deneme, Mechanical and microstructural properties of alkali-activated slag and slag + fly ash mortars exposed to high temperature, Constr. Build. Mater. 217 (2019) 50–61, https://doi.org/10.1016/j.conbuildmat.2019.05.055.
[19] M. Guerrieri, J.G. Sanjayan, Behavior of combined fly ash/slag-based geopolymers when exposed to high temperatures, Fire Mater. 34 (2010) 163–175, https://doi.org/10.1002/fam.1014.
[20] Z. Pan, Z. Tao, Y.-F. Cao, R. Wuhrer, Measurement and prediction of thermal properties of alkali-activated fly ash/slag binders at elevated temperatures, Mater. Struct. 51 (2018) 108, https://doi.org/10.1617/s11527-018-1233-9.
[21] Z. Pan, Z. Tao, Y.F. Cao, R. Wuhrer, T. Murphy, Compressive strength and microstructure of alkali-activated fly ash/slag binders at high temperature, Cem. Concr. Compos. 86 (2018) 9–18, https://doi.org/10.1016/j.cemconcomp.2017.09.011.
[22] M. Lahoti, K.K. Wong, K.H. Tan, E.-H. Yang, Effect of alkali cation type on strength endurance of fly ash geopolymers subject to high temperature exposure, Mater. Des. 154 (2018) 8–19, https://doi.org/10.1016/j.matdes.2018.05.023.
[23] M. Lahoti, S.F. Wijaya, K.H. Tan, E.-H. Yang, Tailoring sodium-based fly ash geopolymers with variegated thermal performance, Cem. Concr. Compos. 107 (2020), 103507, https://doi.org/10.1016/j.cemconcomp.2019.103507.
[24] S.M. Park, J.G. Jang, N.K. Lee, H.K. Lee, Physicochemical properties of binder gel in alkali-activated fly ash/slag exposed to high temperatures, Cem. Concr. Res. 89 (2016) 72–79, https://doi.org/10.1016/j.cemconres.2016.08.004.
[25] A. Sabbatini, L. Vidal, C. Pettinari, I. Sobrados, S. Rossignol, Control of shaping and thermal resistance of metakaolin-based geopolymers, Mater. Des. 116 (2017) 374–385, https://doi.org/10.1016/j.matdes.2016.12.039.
[26] W.D.A. Rickard, C.S. Kealley, A. van Riessen, Thermally induced microstructural changes in Fly ash geopolymers: experimental results and proposed model, J. Am. Ceram. Soc. 98 (2015) 929–939, https://doi.org/10.1111/jace.13370.
[27] M. Dudek, M. Sitarz, Analysis of changes in the microstructure of geopolymer mortar after exposure to high temperatures, Materials 13 (2020) 4263, https://doi.org/10.3390/ma13194263.
[28] X. Gao, Q.L. Yu, A. Lazaro, H.J.H. Brouwers, Investigation on a green olivine nano-silica source based activator in alkali activated slag-fly ash blends: reaction kinetics, gel structure and carbon footprint, Cem. Concr. Res. 100 (2017) 129–139, https://doi.org/10.1016/j.cemconres.2017.06.007.
[29] X.Y. Zhuang, L. Chen, S. Komarneni, C.H. Zhou, D.S. Tong, H.M. Yang, W.H. Yu, H. Wang, Fly ash-based geopolymer: clean production, properties and applications, J. Clean. Prod. 125 (2016) 253–267, https://doi.org/10.1016/j.jclepro.2016.03.019.
[30] F. Qu, W. Li, Z. Tao, A. Castel, K. Wang, High temperature resistance of fly ash/GGBFS-based geopolymer mortar with load-induced damage, Mater. Struct. 53 (2020) 111, https://doi.org/10.1617/s11527-020-01544-2.
[31] N.K. Lee, K.T. Koh, G.H. An, G.S. Ryu, Influence of binder composition on the gel structure in alkali activated fly ash/slag pastes exposed to elevated temperatures, Ceram. Int. 43 (2017) 2471–2480, https://doi.org/10.1016/j.ceramint.2016.11.042.
[32] F. Fan, Z. Liu, G. Xu, H. Peng, C.S. Cai, Mechanical and thermal properties of fly ash based geopolymers, Constr. Build. Mater. 160 (2018) 66–81, https://doi.org/10.1016/j.conbuildmat.2017.11.023.
[33] R. Cai, H. Ye, Clinkerless ultra-high strength concrete based on alkali-activated slag at high temperatures, Cem. Concr. Res. 145 (2021), 106465, https://doi.org/10.1016/j.cemconres.2021.106465.
[34] T. Bakharev, Thermal behaviour of geopolymers prepared using class F fly ash and elevated temperature curing, Cem. Concr. Res. 36 (2006) 1134–1147, https://doi.org/10.1016/j.cemconres.2006.03.022.
[35] D.L.Y. Kong, J.G. Sanjayan, Effect of elevated temperatures on geopolymer paste, mortar and concrete, Cem. Concr. Res. 40 (2010) 334–339, https://doi.org/10.1016/j.cemconres.2009.10.017.
[36] L. Griffiths, M.J. Heap, P. Baud, J. Schmittbuhl, Quantification of microcrack characteristics and implications for stiffness and strength of granite, Int. J. Rock Mech. Min. Sci. 100 (2017) 138–150, https://doi.org/10.1016/j.ijrmms.2017.10.013.
[37] A. Arena, C. Delle Piane, J. Sarout, A new computational approach to cracks quantification from 2D image analysis: application to micro-cracks description in rocks, Comput. Geosci. 66 (2014) 106–120, https://doi.org/10.1016/j.cageo.2014.01.007.
[38] C. Delle Piane, A. Arena, J. Sarout, L. Esteban, E. Cazes, Micro-crack enhanced permeability in tight rocks: an experimental and microstructural study, Tectonophysics 665 (2015) 149–156, https://doi.org/10.1016/j.tecto.2015.10.001.
[39] D.M. Etter, Introduction to MATLAB, 2nd ed, Prentice Hall, Upper Saddle River, NJ, 2011.
[40] ASTM C597-16, Test Method for Pulse Velocity Through Concrete, ASTM International, 2016, https://doi.org/10.1520/C0597-16.
[41] British Standards Institution, London, Methods of testing cement. Part 1, Part 1, 2016.

[42] C.K. Yip, G.C. Lukey, J.S.J. van Deventer, The coexistence of geopolymeric gel and calcium silicate hydrate at the early stage of alkaline activation, Cem. Concr. Res. 35 (2005) 1688–1697, https://doi.org/10.1016/j.cemconres.2004.10.042.
[43] D. Nasr, A.H. Pakshir, H. Ghayour, The influence of curing conditions and alkaline activator concentration on elevated temperature behavior of alkali activated slag (AAS) mortars, Constr. Build. Mater. 190 (2018) 108–119, https://doi.org/10.1016/j.conbuildmat.2018.09.099.
[44] P.W.J. Glover, P. Baud, M. Darot, P.G. Meredith, S.A. Boon, M. LeRavalec, S. Zoussi, T. Reuschlé, α/β phase transition in quartz monitored using acoustic emissions, Geophys. J. Int. 120 (1995) 775–782, https://doi.org/10.1111/j.1365-246X.1995.tb01852.x.
[45] S.A. Bernal, R.M. de Gutierrez, J.L. Provis, V. Rose, Effect of silicate modulus and metakaolin incorporation on the carbonation of alkali silicate-activated slags, Cem. Concr. Res. 40 (2010) 898–907, https://doi.org/10.1016/j.cemconres.2010.02.003.
[46] X. Gao, Q.L. Yu, H.J.H. Brouwers, Reaction kinetics, gel character and strength of ambient temperature cured alkali activated slag–fly ash blends, Constr. Build. Mater. 80 (2015) 105–115, https://doi.org/10.1016/j.conbuildmat.2015.01.065.
[47] P. Rovnaník, P. Bayer, P. Rovnaníková, Characterization of alkali activated slag paste after exposure to high temperatures, Constr. Build. Mater. 47 (2013) 1479–1487, https://doi.org/10.1016/j.conbuildmat.2013.06.070.
[48] W.D.A. Rickard, J. Temuujin, A. van Riessen, Thermal analysis of geopolymer pastes synthesised from five fly ashes of variable composition, J. Non-Cryst. Solids 358 (2012) 1830–1839, https://doi.org/10.1016/j.jnoncrysol.2012.05.032.
[49] L.M. Anovitz, D.R. Cole, Characterization and analysis of porosity and pore structures, Rev. Mineral. Geochem. 80 (2015) 61–164, https://doi.org/10.2138/rmg.2015.80.04.
[50] S. Diamond, Mercury porosimetry: an inappropriate method for the measurement of pore size distributions in cement-based materials, Cem. Concr. Res. 30 (2000) 1517–1525, https://doi.org/10.1016/S0008-8846(00)00370-7.
[51] H. Ma, Mercury intrusion porosimetry in concrete technology: tips in measurement, pore structure parameter acquisition and application, J. Porous. Mater. 21 (2014) 207–215, https://doi.org/10.1007/s10934-013-9765-4.
[52] Q. Zeng, K. Li, T. Fen-chong, P. Dangla, Pore structure characterization of cement pastes blended with high-volume fly-ash, Cem. Concr. Res. 42 (2012) 194–204, https://doi.org/10.1016/j.cemconres.2011.09.012.
[53] K.K. Aligizaki, Pore Structure of Cement-Based Materials: Testing, Interpretation and Requirements, CRC Press, 2005.
[54] D.H. Everett, Manual of symbols and terminology for physicochemical quantities and units, appendix II: definitions, terminology and symbols in colloid and surface chemistry, Pure Appl. Chem. 31 (1972) 577–638, https://doi.org/10.1351/pac197231040577.
[55] N.K. Lee, J.G. Jang, H.K. Lee, Shrinkage characteristics of alkali-activated fly ash/slag paste and mortar at early ages, Cem. Concr. Compos. 53 (2014) 239–248, https://doi.org/10.1016/j.cemconcomp.2014.07.007.
[56] Z.Y. Qu, Q. Yu, Y.D. Ji, F. Gauvin, I.K. Voets, Mitigating shrinkage of alkali activated slag with biofilm, Cem. Concr. Res. 138 (2020), 106234, https://doi.org/10.1016/j.cemconres.2020.106234.
[57] H. Ye, C. Cartwright, F. Rajabipour, A. Radlińska, Understanding the drying shrinkage performance of alkali-activated slag mortars, Cem. Concr. Compos. 76 (2017) 13–24, https://doi.org/10.1016/j.cemconcomp.2016.11.010.
[58] I. Ismail, S.A. Bernal, J.L. Provis, R.San Nicolas, S. Hamdan, J.S.J. van Deventer, Modification of phase evolution in alkali-activated blast furnace slag by the incorporation of fly ash, Cem. Concr. Compos. 45 (2014) 125–135, https://doi.org/10.1016/j.cemconcomp.2013.09.006.
[59] A. Fernández-Jiménez, J.Y. Pastor, A. Martín, A. Palomo, High-temperature resistance in alkali-activated cement, J. Am. Ceram. Soc. 93 (2010) 3411–3417, https://doi.org/10.1111/j.1551-2916.2010.03887.x.
[60] K. Behfarnia, M. Shahbaz, The effect of elevated temperature on the residual tensile strength and physical properties of the alkali-activated slag concrete, J. Build. Eng. 20 (2018) 442–454, https://doi.org/10.1016/j.jobe.2018.08.015.